2022

Verification of Electron Beam Production for Radiation Dosimetry Experimentation

Henri J. LeMieux
Minnesota State University, Mankato

VERIFICATION OF ELECTRON BEAM PRODUCTION FOR RADIATION DOSIMETRY EXPERIMENTATION

by

Henri J. LeMieux

A thesis submitted in partial fulfillment of the requirements for

Master of Science in Physics

Minnesota State University, Mankato

Mankato, Minnesota

July 2022

ENDORSEMENTS/SIGNATURE PAGE

Date: 06/27/2022

This paper is submitted as part of the required work for the degree of MS in Physics at Minnesota State University – Mankato, and has been supervised, examined, and accepted.

Examining Committee:

_____

Dr. Andrew Roberts (Advisor)

_____

Dr. Analía Dall'Asén (Committee Member)

_____

Dr. Thomas Brown (Committee Member)

ACKNOWLEDGEMENTS

Special thanks to my advisor, Dr. Andrew Roberts, for being a mentor during my time as a Maverick. His patience, understanding, and knowledge were a huge help to me as I fulfilled my dream of studying nuclear/medical physics. Thanks to Dr. Analía Dall'Asén and Dr. Jorge Méndez for all their help, guidance, and support in making graduate school a lot less stressful. From conversations in the hallway to physics club get-togethers, their ability to form a friendly relationship with students has been unmatched in my academic experience. Thank you to Cindy Flitter and Mike Peters, for helping with documents, emails, and technical problems. A further thanks to all the physics and astronomy professors. Everyone had their own unique style of teaching physics, and all that I've learned from them will be something I hope to take with me wherever I end up.

My time in Mankato would not have been the same if not for my friends and family. Thanks to David M., Jackson W., Preston F., and Samantha S., for aiding in this study. Thank you to T.J. Gehrman for encouraging me to attend graduate school at MSU. Thank you to Wasiu Erinoso and Meredith Rupp for being my office mates and putting up with me. And a further thank you to all the other physics and astronomy students I've interacted with during my time here. The memories will stay with me forever. A special thanks to my parents and sisters for encouraging me to chase my passions. Thank you to my grandmother, Marion DeGroot, for helping to put me on this path early in life by getting me interested in math and science when I was five years old.

And lastly, to my moon, Selene J. Prince, for being the light of my life, shining bright when things seem dark. Being physically apart for the past four years has been rough, but the daily phone calls kept me going and helped me to reach this point. We can now be reunited and plan our future together. The next adventure awaits!

TABLE OF CONTENTS

Abstract

Radiation is a natural phenomenon in which energy is emitted in the form of waves or particles through a given medium. Radiation dosimetry is the method of analyzing and assessing this deposited emitted energy. How this emitted energy effects a given object when deposited has been a topic of interest in the fields of science and medicine. In this paper, a novel method is proposed for the verification of electrons in air and determining their delivered dose rate.

Using a linear accelerator which had its polarity flipped from producing positive ions to producing electrons, work to verify the production of electrons is undertaken. A Geiger-Mueller counter with a fixed radioactive reference source is used. Count rates are taken for various distances with results being compared with predictions using data obtained from the NIST-ESTAR database. Angular distribution is investigated using a similar method. Further work is conducted using Helmholtz coils to control beam direction via uniform magnetic field. Using a radiation safety badge at a given distance, a preliminary dose rate measurement is obtained.

A novel approach to validate the production of electrons is achieved. At distances of 80 *cm*, 90 *cm*, and 100 *cm*, oriented at 0°, kinetic energies of 315±5 *keV*, 345±5 *keV*, and 360±5 *keV*, respectively, are measured. For the same distances, an increase in required kinetic energy is measured when the detector is oriented at an angle. At a distance of 100 *cm* oriented at 45°, a kinetic energy of 380±5 *keV* is measured, an increase from the 0° orientation. Results are consistent with distance calculations using data for electrons in dry air obtained from the NIST-ESTAR database, given for orientation at 0°. Preliminary results using Helmholtz coils for beam control show promise, but suggest further investigation is required. Radiation safety badge data shows 5-minute exposure to the beam energy exceeds the badge limit of 1000 *Rad.*, demonstrating delivery of a high radiation dose.

Chapter One

Introduction

1.1 Background of the Study

Radiation is a natural phenomenon in which energy is emitted in the form of electromagnetic waves or particles through a given medium. In radioactive processes, particles or electromagnetic radiation are emitted from the nucleus. The most common forms of emitted radiation were classified by Ernest Rutherford and Paul Villard as alpha (α), beta (β), and gamma (γ) radiation. Nuclear radiation occurs by means of other methods such as the emission of protons or neutrons, or through spontaneous fission of a massive nucleus. The majority of all nuclei found on Earth today are considered stable. This is because nearly all short-lived radioactive nuclei have decayed since the Earth first formed. Today there are over 3,000 known isotopes, approximately 270 of which are stable, and many of which are created within laboratories. Atomic nuclei which are known as unstable spontaneously decay until eventually reaching a stable state. Radioactive decay changes one nucleus into another, and the product nucleus will have a greater binding energy than the initial decaying nucleus. This difference in binding energy determines which decays are energetically possible and which are not. An excess in binding energy comes in the form of kinetic energy or rest-mass energy of the decay product.

Radiological physics is the study of ionizing radiation and its interaction with matter, particularly in the absorbed energy. Radiation dosimetry is the quantitative determination of that energy. Radiological physics began with the discovery of x-rays by Wilhelm Röntgen in 1895. Within years x-rays became a useful tool in the field of

medicine, specifically diagnostic radiography. By the end of the 1920's, with the invention of multiple accelerators, the field of radiological physics was further expanded, allowing for the production of lab-based particles of controllable energy, intensity, and direction (Bygrave 1970). By the end of World War II, the field of radiological physics had expanded to the development of safe and reliable treatments for cancer with radiation and quantification of radiation dose that is required to evaluate the therapeutic effect (Masahiro 2021).

The natural background radiation of the Earth along with cosmic rays have been one of the key environmental factors which have affected the rate of evolutionary processes (Møller 2012, Shahbazi-Gahrouei, Setayandeh, and Gholami 2013). Ionizing radiations can influence cells, causing mutations and damage to DNA. This results from both direct and indirect effects of radiation. Biological systems such as the human body are particularly susceptible to damage from ionizing radiations. The ability of ionizing radiations to impart their energy to individual atoms, molecules, and biological cells has a profound effect on the outcome (Attix 1986). Ionizing radiations also have an impact on crystalline materials, desirable or not, by causing defects within the lattice structure.

1.2 Objectives

The goals of this paper are to establish a method for irradiating samples with beta radiation using a linear accelerator and determine the radiation dose rate for the purpose of studying the effects on a given material, organic or non-organic. Previous work was

conducted to reverse the polarity of the accelerator, originally producing a beam of positive ions, to producing a beam of electrons. Important questions to answer are:

(1) Is the accelerator producing electrons?

(2) Can a dose rate be determined?

(3) Can a magnetic field, primarily a small pair of Helmholtz coils, be used to control the directionality of the beam?

1.3 Significance of the Study

There has been a growing interest in utilizing radiation over the years within laboratories, industries, militaries, hospitals, and universities. Hospitals, doctors, and researchers make use of radiation for diagnostics, and monitoring/treating a wide variety of medical conditions within biological organisms. Within industry the use of radiation varies widely, from irradiating foods, improving freshness and lifespan, to determining the moisture and density of soils and materials at construction sites. Throughout these professions it is imperative to know the delivered dose rate of radiation in order to ensure the safety of the necessary materials and the workers involved. Many radiation workers are unavoidably exposed to prolonged exposure of radiation, thus making it increasingly important to determine the delivered dose rate and evaluate the biological effects of radiation on humans/animals.

Chapter Two

Literature Review

2.1 Types of Ionizing Radiation

There are two main forms of radiation: ionizing and non-ionizing. Ionizing radiation is the act of an incoming particle or electromagnetic wave with sufficiently high energy interacting with an atom, causing an electron to branch off the atom. A few examples of ionizing radiation are x-ray machines, and radioactive elements like uranium. Non-ionizing radiation is the act of an incoming particle or electromagnetic wave interacting with an atom, where there is enough energy to potentially cause the atom (or molecule) to move around, or vibrate, but not enough energy to cause an electron to break off. A few examples of non-ionizing radiation include radio antenna, and microwave machines. The study of radiological physics and nuclear physics focuses primarily on ionizing radiation.

Evidence for radioactivity began in 1896 with Henri Becquerel while investigating how uranium salts are affected by light. Becquerel demonstrated that uranium salts spontaneously emit a penetrating radiation which can be registered by a photographic plate. Expanding on Becquerel's discovery, in 1899 Ernest Rutherford demonstrated there are two distinct types of ionizing radiation: alpha and beta. The next year, in 1900, chemist Paul Villard discovered the third type of ionizing radiation, aptly labeled gamma. The classification of these three types of ionizing radiation are based on their ability to excite and ionize matter, and their ability to penetrate materials. Figure 2.1 shows the typical penetration depth of the three types of radiation. There are other kinds of particles used in

particle accelerators such as protons, neutrons, deuterons, heavy ions, and micro- and macroparticles. Many of these other particles require careful explanation outside the purview of this study so they'll only be mentioned and not expanded upon.

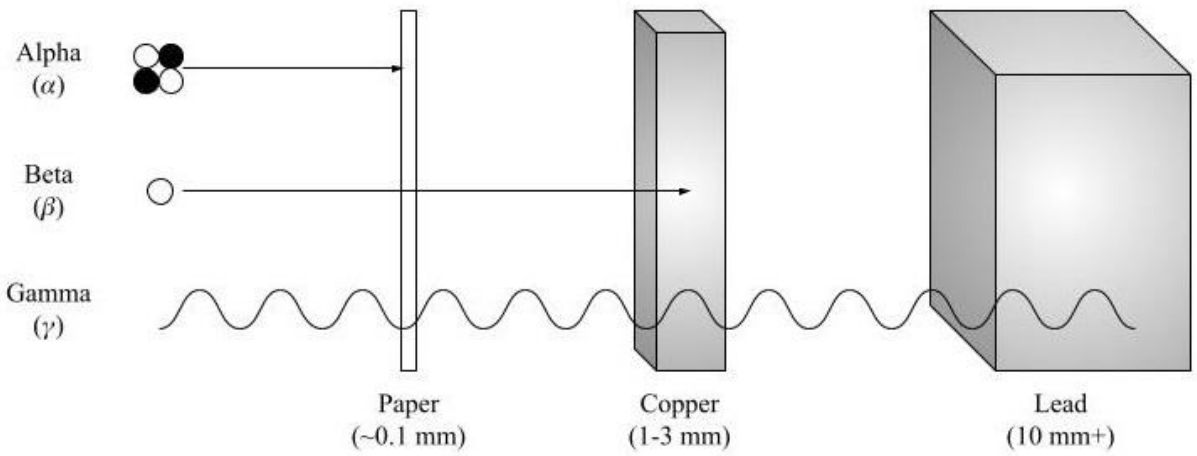

Figure 2.1: Basic penetration depth of the three common types of ionizing radiation.

Alpha radiation (α) is a class of heavy charged particle consisting of two protons and two neutrons bound together as ^{4}He, typically obtained from acceleration by a Coulomb force field, or radioactive decay. Alpha rays were defined by Rutherford has having the lowest penetration depth of ordinary objects and shortest range in air, where a standard sheet of paper has sufficient thickness to block an alpha ray (See Figure 2.1). Due to the short range of absorption and inability to penetrate the outer layers of skin, alpha particles are not, in general, dangerous to life unless the source is either ingested or inhaled (Christensen et. al. 2014). Alpha rays are considered to be the most destructive type of radiation, however, to biological systems in equivalent activity due to their large size, short range, long half-life and decay rate.

Gamma radiation (γ) is electromagnetic radiation emitted from a nucleus or in annihilation reaction between matter and antimatter (Attix 1986). Gamma rays and x-rays occupy the same region on the electromagnetic spectrum and are distinguishable only by their origin. Gamma rays result from nuclear transitions, and x-rays result from interactions with electrons outside the nucleus. It is often convenient to assign wavelike properties to x and gamma rays (Hendee 1970). At other times it is useful to regard these radiations as discrete bundles of energy termed photons or quanta (Franck 1957). Gamma rays are capable of traveling long distances at the speed of light and have great ability to penetrate materials (see Figure 2.1). Gamma rays are often used in medical applications to treat cancer and sterilize medical instruments and x-rays are typically used to provide static images of body parts such as teeth and bones (US NRC 2017). While gamma rays can penetrate most materials, they do not have the ability to make anything radioactive. It takes dense material such as lead with a thickness of 10+ *mm* to block gamma rays.

Beta radiation (β) consists of a high-energy, high-speed electron (β^-, or e^-) or positron (β^+, or e^+) which are emitted through radioactive decay, or electrostatically generated within charged particle accelerators. Beta particles are lighter than alpha particles, allowing them to traverse a medium further and penetrate materials deeper. While alpha particles can be stopped by a thin sheet of paper, beta particles with sufficient energy will pass through a sheet of paper but halt within less than a few millimeters in material like copper (see Figure 2.1). In general, beta particles are capable of penetrating human skin, but incapable of penetrating bone, making them useful in treating medical conditions such as eye and bone cancers. Strontium-90 is the most used material to produce beta particles through radioactivity, while a Van de Graaff particle accelerator can generate a

beam of electrons. This study is focused on beta radiation generated using a Van de Graaff particle accelerator.

2.2 Van de Graaff Particle Accelerator

During the early years of nuclear study, most experiments were conducted using nuclear material such as radium, polonium, and thorium. At that time, nuclear material for research was in short supply, with researchers refusing to share as much as half a gram of radium (Bygrave 1970). By the 1920's there were calls for laboratory-accelerated particles of controllable energy, intensity, and direction. Around 1930 multiple accelerators were proposed to meet these requirements. These accelerators included Cockcroft-Walton, the linear accelerator, the cyclotron, and the Van de Graaff.

The Van de Graaff particle accelerator was invented in 1931 by Robert J. Van de Graaff. The first nuclear physics experiment using a Van de Graaff accelerator was in 1935 by M. Tuve, after which the accelerator established itself as the best option for nuclear structure research due to its effectiveness at delivering a well-defined beam of precisely known energy which can be readily changed (Bygrave 1970).

The main operation of the Van de Graaff accelerator consists of three important steps: generation of a high D.C. potential; production and acceleration of a beam of either positive ions or electrons (depending on positive or negative potential); measurement and management of beam energy. Referring to Figure 2.2, in Dr. Waldemar Scharf's book "Particle Accelerators and Their Uses", he explains the Van de Graaff accelerator contains a device for charging a conveyor belt. Close to this belt is a needle point which acts as an

emitter. Under the influence of a strong electric field, positive and negative ions are produced within a gaseous medium surrounding the point. If the needle point has a negative potential, this point will repel negative ions which get deposited on the surface of the belt. These charges are distributed uniformly on the surface of the belt and carried upward into the terminal. Inside the spherical electrode is another needle point called the charge collector. This charge collector picks up the generated charges from the belt surface and transports them to the surface of the terminal, which thus acquires an ever-increasing potential. Figure 2.2 displays a terminal charged to a positive potential coming from a positive potential in the charge supply. If the charge supply were to have a negative potential the terminal would be charged negatively.

Inside of the terminal another needle point which functions like the charge supply at the bottom of the pulley. This prevents the belt from returning "empty-handed" as it traverses from the upper pulley back toward the lower pulley. The needle point within the terminal sprays charges onto the belt, opposite the charges being collected, which are then carried to the bottom pulley. If the polarity of the charge supply were to be reversed, then the polarity of the terminal will also be reversed (Scharf 1996).

The pressure tank housing the accelerator components is filled with insulating gases at a pressure around 100 psig as a means of providing high-voltage insulation, preventing discharges, or "sparks". These insulating gases are nitrogen (~45%), carbon dioxide (~50%), and occasionally sulfur hexafluoride (~5%) which has the highest dielectric strength with the drawback of having a corrosive effect on the accelerator parts made of organic materials.

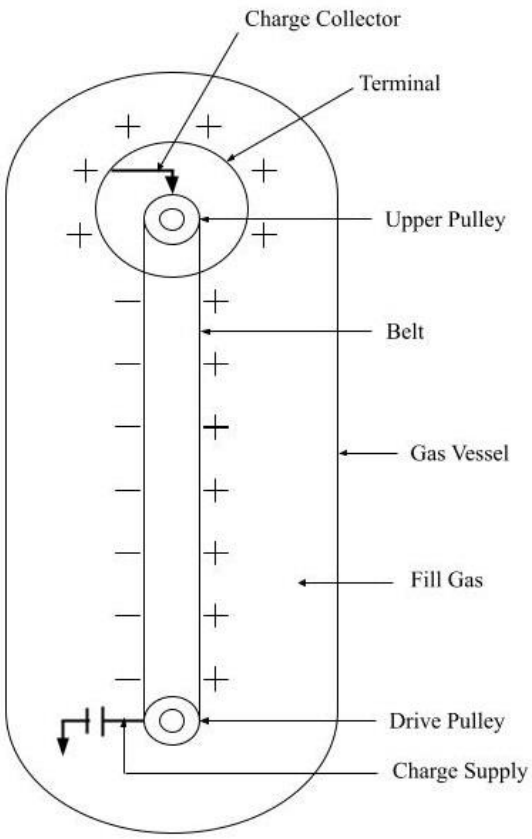

Figure 2.2: Construction of a Van de Graaff Accelerator, displaying the production of positive ions

Not pictured within Figure 2.2, but worth briefly mentioning, is the ion source. Enclosed within the terminal is a radio-frequency ion source and electronics necessary for operation. A gas, such as hydrogen, flows into a source bottle where it will be ionized via radio-frequency energy. Permanent magnets placed symmetrically around the ion source provide an axial magnetic field, restricting the paths of the electrons, thus increasing the probability of ionization per electron released from the source (Bygrave 1970). Extraction of the ions through an exit occurs by applying a voltage to the probe fixed at top of the source bottle. These extracted ions are then accelerated to upwards of 400 *keV* (for the

given Van de Graaff accelerator) by a uniform voltage gradient applied to the acceleration tube (Bygrave 1970).

2.3 Stopping Power and CSDA Range

Charged particles lose their energy in a different manner compared to uncharged particles (such as gamma rays and x-rays). A gamma ray such as a photon incident on a material may pass through it without an interaction, thus losing no energy, or interact and lose its energy within one or a few events. A charged particle, by contrast, being surrounded by its Coulomb electric force field, interacts with one or more electrons or with the nucleus of practically every atom it encounters (Attix 1986). Most interactions will only transfer fractions of the incident particle's kinetic energy, and it can be viewed as the particle losing its kinetic energy gradually, in a process referred to as the continuous slowing-down approximation, abbreviated CSDA. There is near zero chance a charged particle will ever pass through a material with no interactions occurring. A 1 *MeV* particle will typically undergo ~10^5 interactions before losing all its kinetic energy (Attix 1986).

Charged particles can be crudely characterized by a common pathlength, traced out by the specific particle and energy in a given medium. Due to the number of interactions a charged particle will undergo in slowing down, its pathlength will approach the expectation value which would be the average for a large population of similar charged particles. This expectation value is considered the range. All identical charged particles will not travel along the same path, and the traveled paths are not necessarily linear.

The stopping power of charged particle in a given medium can be defined as the energy loss for that particle within the medium divided by the differential pathlength, or,

$$S = -\frac{dE}{dx}$$

which is commonly referred to as the rate of energy loss. The classical expression which describes this energy loss is known as the Bethe formula, expressed as

$$-\frac{dE}{dx} = \frac{4\pi e^4 z^2}{m_0 v^2} NB$$

where

$$B \equiv Z\left[ln\frac{2m_0v^2}{I} - ln\left(1-\frac{v^2}{c^2}\right) - \frac{v^2}{c^2}\right]$$

Here, ze is the charge of the particle, v is the velocity of the particle, N is the number density, Z is the atomic number of the absorber atoms, m_0 is the electron rest mass, e is the electronic charge, and I is a parameter representing the average excitation and ionization potential of the absorber which is experimentally determined for each element. Electrons lose their energy at a lower rate compared to heavy charged particles and follow more tortuous paths through a given absorbing medium. Bethe, two years after his classical derivation, expanded on his classical formula by deriving a new expression to describe the specific energy loss due to ionization and excitation (Collisional losses) for relativistic electrons:

$$-\left(\frac{dE}{dx}\right)_c = \frac{2\pi e^4 NZ}{m_0 v^2}\left(ln\frac{m_0 v^2 E}{2I^2(1-\beta^2)}\right.$$

$$\left. -(\ln 2)\left(2\sqrt{1-\beta^2}-1+\beta^2\right)+(1-\beta^2)+\frac{1}{8}(1-\sqrt{1-\beta^2})^2\right)$$

with the same symbols to the classical equation, and the inclusion of the relativistic term $\beta \equiv v/c$.

Energy from electrons may also be lost by radiative processes and by coulomb interactions. These losses take the form of bremsstrahlung or electromagnetic radiation. This loss can occur at any point along the electron path. Any charge must radiate energy when accelerated, and the interactions of the electron with the absorber corresponds to an acceleration. The energy loss from this radiative process is

$$-\left(\frac{dE}{dx}\right)_r = \frac{NEZ(Z+1)e^4}{137m_0^2c^4}\left(4\ ln\frac{2E}{m_0c^2}-\frac{4}{3}\right)$$

The radiative loss equation is most important for high electron energies and for absorber materials of large atomic number. For typical electron energies, the average bremsstrahlung photon energy is quite low and therefore normally reabsorbed close to its point of origin (Knoll 2010). The total stopping power for electrons is therefore the sum of the collisional and radiative losses, giving

$$\frac{dE}{dx} = \left(\frac{dE}{dx}\right)_c + \left(\frac{dE}{dx}\right)_r$$

Dividing the stopping power by the density ρ of the absorbing medium gives a quantity referred to as mass stopping power $(dE/\rho dx)$, which is now dependent on both the properties of the incident particle and the density of the absorber material, with units

$MeV\ cm^2/g$. The quantity of mass stopping power is often used in research environments and is a useful quantity to determine the range of charged particles, like electrons.

Knowing the mass stopping power allows for the calculation of the range of a charged particle. The range (R) of a charged particle of a given type and energy in a given medium is the expectation value of the pathlength that it follows until it comes to rest (Attix 1986). The projected range of a charged particle of a given type and initial energy in a given medium is the expectation value of the farthest depth of penetration of the particle from its initial direction (Attix 1986). A similar quantity for range is known as the CSDA range (R_{CSDA})(Berger and Seltzer 1983). For practical purposes, R_{CSDA} is comparable to R, with only a subtle difference due to the occurrence of discrete and continuous energy losses. This subtle difference leads to R_{CSDA} being a slight underestimate of the actual range by 0.2% for protons, and a larger, yet unknown, percentage for electrons. In terms of the mass stopping power, the CSDA range, R_{CSDA}, is defined as

$$R_{CSDA} \equiv \int_0^{E_0} \left(\frac{dE}{\rho dx}\right)^{-1} dE$$

where E_0 is the is the initial energy of the particle. The units of R_{CSDA} are g/cm^2.

Today most data referring to mass stopping power and CSDA ranges may be looked up in various databases online, with each database relating to a specific charged particle. The National Institute of Standards and Technology (NIST) keeps a database of mass stopping powers and CSDA ranges for electrons of a given energy traversing various mediums, known as the electron stopping power and range database (ESTAR). A similar database exists for protons (PSTAR), as well as alpha particles (ASTAR). Within this

database, one can choose a material with which to see collected data of mass stopping power and CSDA range. Table 2.1 refers to a small cutout of data for electrons in dry air. Kinetic energy within this database ranges from 10 *keV* up to 1 *GeV* in varying increments. ESTAR also displays a graph of the range as a function of electron energy, showing how the range varies with energy as the electrons traverse through the given medium of choice. Figure 2.3 shows a graph of the range of an electron as a function of energy through dry air.

Kinetic Energy (MeV)	**Stopping Power (MeV cm^2/g)**			**CSDA (g/cm^2)**	**Radiation Yield**	**Density Effect Parameter**
	Collision	**Radiative**	**Total**			
1.750E-01	2.637E+00	4.633E-03	2.642E+00	4.103E-02	1.006E-03	0.000E+00
2.000E-01	2.469E+00	4.789E-03	2.474E+00	5.082E-02	1.111E-03	0.000E+00
2.500E-01	2.236E+00	5.126E-03	2.241E+00	7.213E-02	1.311E-03	0.000E+00
3.000E-01	2.084E+00	5.495E-03	2.089E+00	9.528E-02	1.502E-03	0.000E+00
3.500E-01	1.978E+00	5.890E-03	1.984E+00	1.199E-02	1.688E-03	0.000E+00
4.000E-01	1.902E+00	6.311E-03	1.908E+00	1.456E-02	1.869E-03	0.000E+00

Table 2.1: Stopping Power and Range Table for electrons in dry air from NIST ESTAR Database

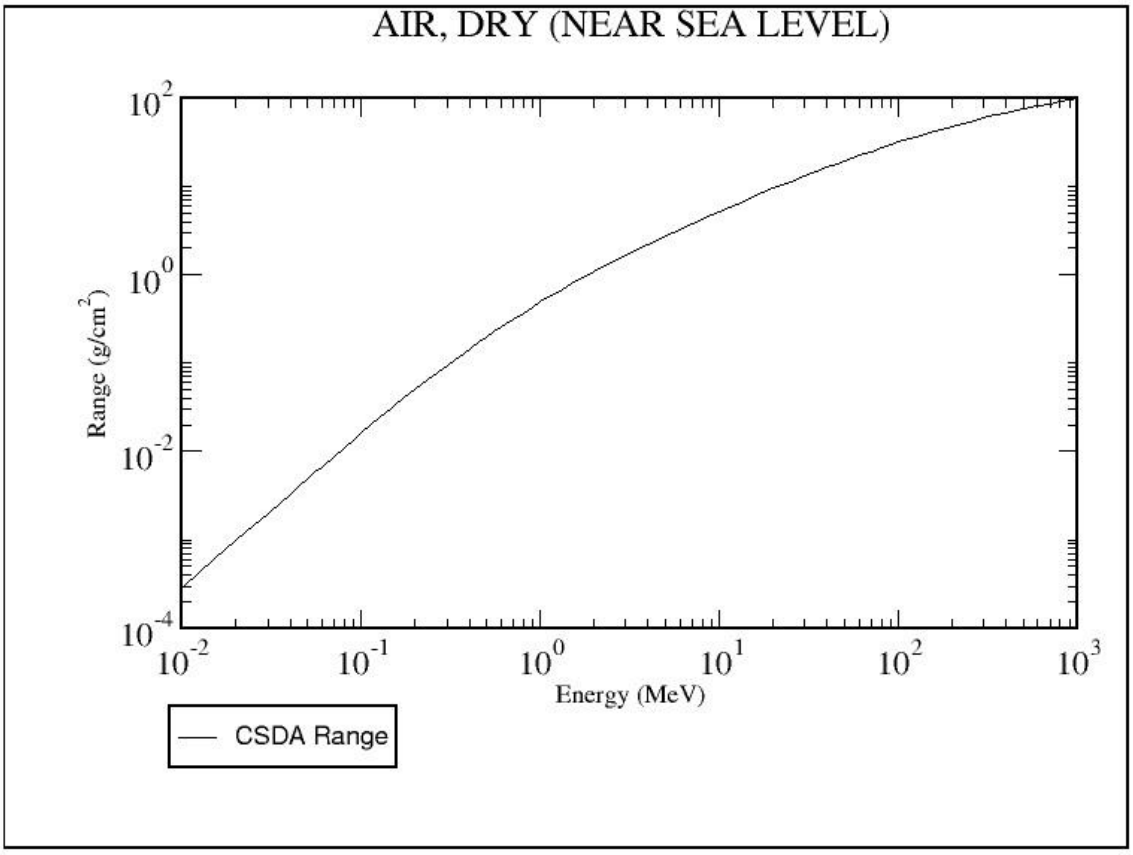

Figure 2.3: Graph of range versus energy of electrons in dry air from the NIST ESTAR Database

In a backward approach, looking up the CSDA range of an electron in a given medium of known density, the distance traveled by an electron before coming to rest can be calculated. The units of R_{CSDA} are g/cm^2, therefore dividing by the density of the medium should yield the distance the electron travels before coming to rest. The equation may be thought of as

$$x = \frac{R_{CSDA}}{\rho}$$

where x is the expected distance the electron will travel before coming to rest. For a 300 *keV* electron traveling in dry air, this would yield a travel distance of

$$x = \frac{9.528 \times 10^{-2}\ g/cm^2}{1.225 \times 10^{-3}\ g/cm^3} = 77.78\ cm$$

Knowing the range of charged particles through a given medium is important when it comes to setting up detecting equipment.

Radiation yield and density effect parameter were beyond the scope of the study and thus are not elaborated on in this paper. A more detailed explanation of each column can be found in chapter 8 of Frank Herbert Attix's book "Introduction to Radiological Physics and Radiation Dosimetry".

2.4 Geiger-Mueller Counters

The Geiger-Mueller (G-M) counter is one of the earliest radiation detectors still used today despite being invented in 1928. Their popularity stems from the simplicity of their design, low cost, and ease of operation. G-M counters have been written on extensively, including reviews by Emery (1966), Price (1964), Sharpe (1964), and Wilkinson (1950), the latter of whom has written a series of works detailing the physical processes involved in Geiger discharge. Further detailed work, spanning several chapters, is also provided by Glenn Knoll in his book "Radiation Detection and Measurement". This section will discuss the characteristics of the G-M counter which make them useful tools for radiation dosimetry.

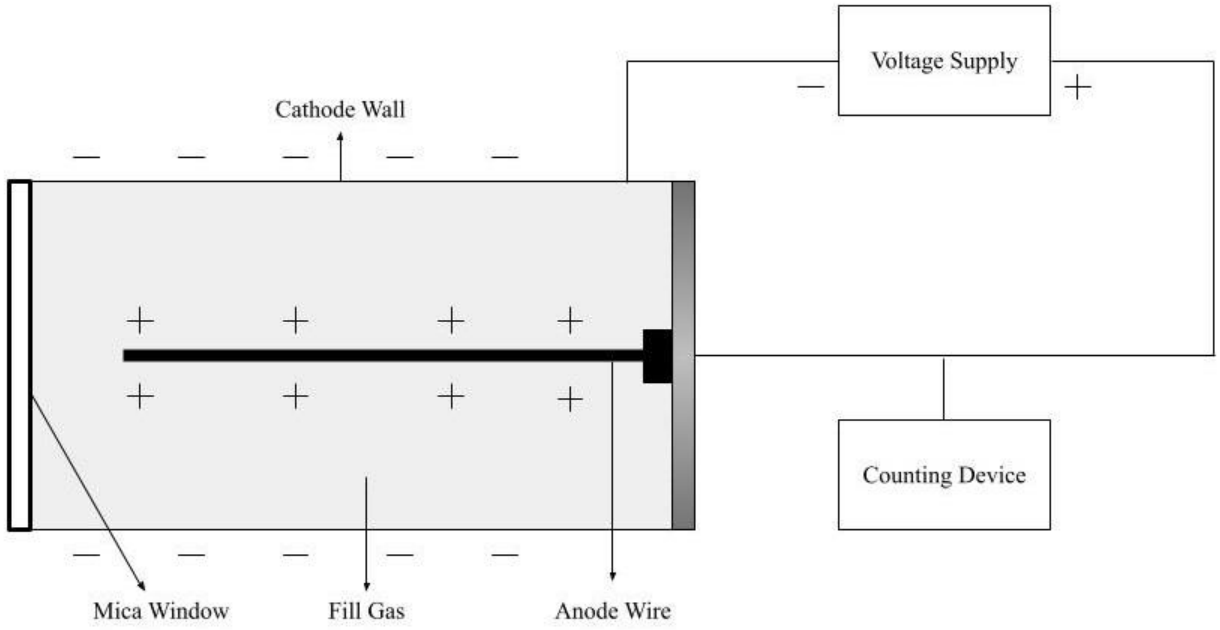

Figure 2.4: Schematic of G-M tube and counter.

A G-M counter has two main components – a sealed tube, which is filled with a noble gas such as argon, and an information display. Figure 2.4 shows the typical setup of a G-M tube and counter. The tube (or ionization chamber) consists of a mica window, a cathode wall, an anode wire, and fill gas. Any ionization chamber with sufficiently good electrical insulation can, in principle, be operated at an applied potential great enough to cause gas multiplication (Attix 1986). This is a condition in which free electrons from ionization events may obtain sufficient kinetic energy from the applied electric field to ionize other gas molecules they collide with. Therefore, a single electron can give rise to what is known as a Townsend avalanche, where the number of free electrons doubles over and over as they fly toward the anode wire. At atmospheric pressure the field strength required for gas multiplication to occur is between 500-2000V (Knoll 2010). In Figure 2.4, the central wire within the tube serves as the anode, connected to the + polarity of the

voltage supply. If it is not, the free electrons produced by radiation within the fill gas would travel outward, away from the wire.

In a typical Townsend avalanche, many excited gas molecules are formed by electron collisions. Excited molecules then return to their ground state through the emission of photons. These photons make up the Geiger discharge. An emitted photon from the inner electron shell may be reabsorbed elsewhere by photoelectric absorption involving an outer electron, thus creating a new free electron. The photon could also reach the cathode wall, releasing a free electron upon absorption. In both cases the newly created free electron will move toward the anode wire, triggering yet another avalanche (see Figure 2.5).

Once the free electrons are "collected" by the anode wire, they will make their way toward the positive terminal of the connected power supply. During this process they will pass through a connected counting device. This device will register the current pulse, adding one count to the display. The counting device goes up by one count for each current pulse.

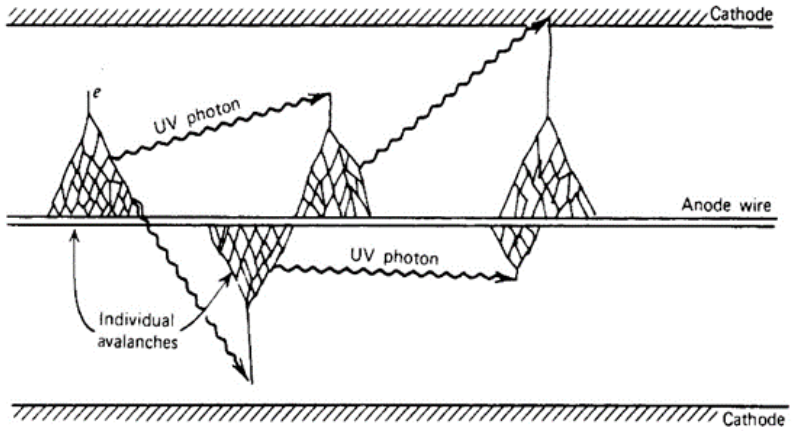

Figure 2.5: The mechanism by which additional avalanches are triggered in a Geiger discharge (Knoll 2010)

Since G-M counters are only triggered by ionizing events which produce pulses roughly the same size, the observed output says little about the dose received by the fill gas. G-M counters are used in dosimetry application since they offer several advantages, according to Attix. They require little amplification, are inexpensive by comparison to other detectors, and are versatile in their construction and geometry. G-M counters are often used in radiation surveys to measure x-ray and gamma ray fields. When a G-M tube is equipped with a thin window they can be used to detect beta rays (Attix 1986).

2.5 Dead Time

In all detector systems, there is a minimum amount of time that must separate two events for them to be recorded by a counter as two separate pulses. This time limitation may be due to the detector and/or the electronics. Overlapping pulses will be recorded by the counting device as a single pulse, lowering the recorded count rate (counts per time). This happens immediately after a discharge when the positive space charge weakens the electric field near the wire, preventing gas multiplication from occurring. The G-M tube will not respond to radiation until the positive ion cloud moves closer toward the cathode and the electric field strength around the wire builds back up. As this is happening, the G-M tube is still capable of responding to an ionization event with a discharge of decreased size (see Figure 2.6).

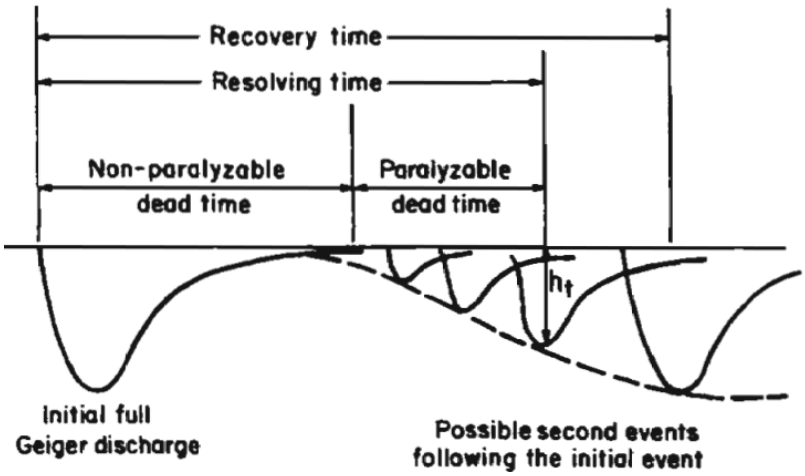

Figure 2.6: Dead time and recovery time of a G-M tube. (Attix 1986)

The true dead time is the time from the initial pulse until a minimum pulse can be generated. The recovery time is when another full-sized pulse can be generated (see Figure 2.6). The minimum time between detectable pulses is less than the recovery time, known as the pulse resolving time, or "dead time". Any event happening during true dead time is not recorded, but the G-M tube is still capable of responding to later events. This is known *nonparalyzable* dead-time behavior. If an ionization event occurs after the true dead time but before a minimum, decreased-height, pulse can be recorded, not only will that event go uncounted, but it will also trigger a new dead time period, and the G-M tube will fail to count any later event before the end of the resolving time. This is known as *paralyzable* dead-time behavior. G-M counters exhibit dead-time behavior which is a mixture of both paralyzable and nonparalyzable. Figure 2.7 demonstrates these concepts.

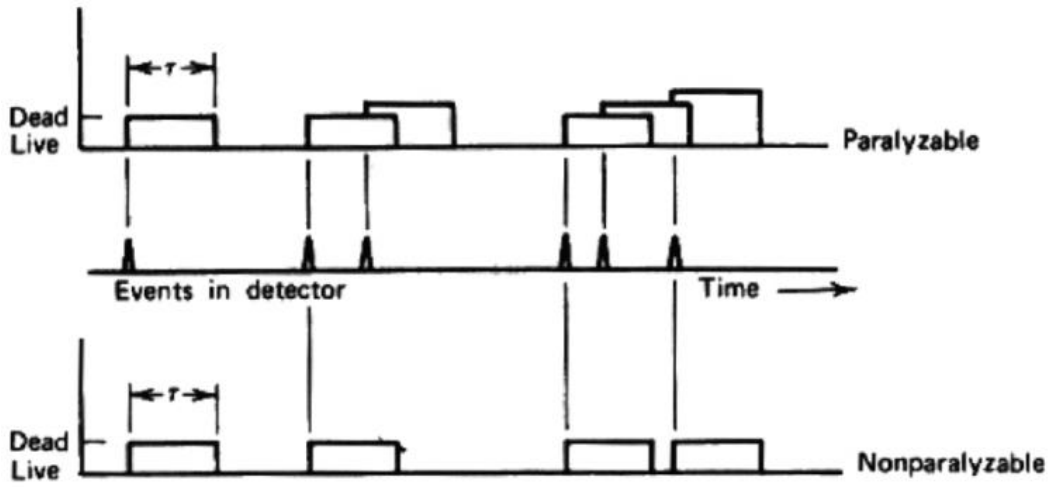

Figure 2.7: Illustration of two models of dead time behavior (Knoll 2010)

It is possible to calculate the true count rate if the observed count rate and pulse resolving time are both known. If we assume m is the observed count rate, n is the true count rate, and τ is the pulse resolving time, for the nonparalyzable case we have

$$n = \frac{m}{1 - m\tau}$$

and for the payalyzable case

$$m = ne^{-n\tau}$$

where n cannot be solved for explicitly. The paralyzable case must be solved for iteratively from measurement of m and τ is known. For low dead-time losses ($n \ll 1/\tau$), both cases reduce to

$$m \cong n(1 - n\tau)$$

The details of lost counts depend on how the pulses from the detector are shaped, processed, or counted, so dead time behavior from measurement systems is dependent on the processing electronics and time characteristics of the detector signals (Knoll 2010). In comparison to other detector devices, G-M tubes are more susceptible to long dead time behavior, which is considered a drawback for many applications, requiring careful planning and setup.

2.6 Magnetic Field from Helmholtz Coils

A Helmholtz coil is defined as either one or two parallel coaxial circular coils in series, separated from each other by a distance equal to the radius of the coils, which produces an approximately uniform magnetic field in the space between the coils (see Figure 2.8). Each coil carries an equal electric current flowing in the same direction. Helmholtz coils are used for a number of reasons. They are often used in certain experiments to cancel out the Earth's magnetic field. Helmholtz coils were used in an experiment to measure the charge to mass ratio (e/m) of electrons and are capable of bending a beam of electrons.

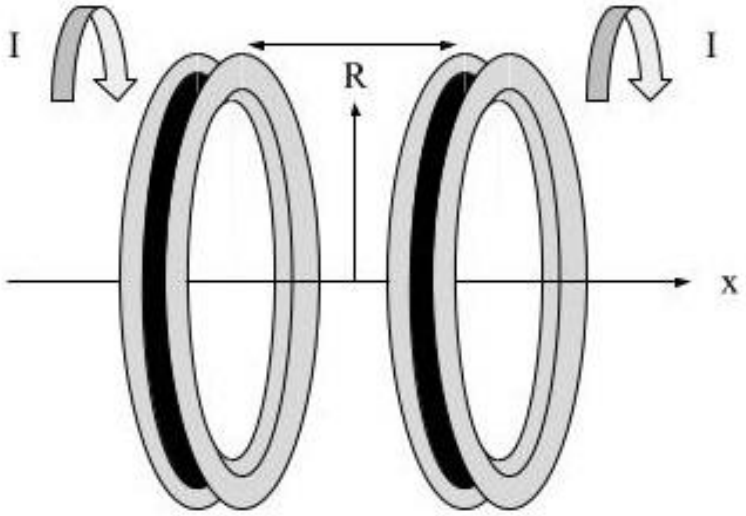

Figure 2.8: Schematic of Helmholtz coils

To calculate the exact value of the magnetic field along the line of axis, x, consider the radius of the coils to be R, the coils comprised of n turns, current through the coils I, magnetic field B, and permeability of free space μ_0 (which is $4\pi \times 10^{-7}\ Tesla \times meter/Ampere$). Beginning with the formula for the on-axis field due to a single n-turn wire and current I, the magnetic field at any point x is

$$B_1(x) = \frac{\mu_0 n I R^2}{2(R^2 + x^2)^{3/2}}$$

which comes from the Biot-Savart Law.

In a Helmholtz coil, consisting of two coils, a point halfway between the two loops has an x-value which is equal to half the separation distance between the coils $(R/2)$, giving

$$B_1\left(\frac{R}{2}\right) = \frac{\mu_0 nIR^2}{2\left(R^2 + \left(\frac{R}{2}\right)^2\right)^{3/2}}$$

Since there are two coils (assume one coil at $x = 0$, and the second coil at $x = R$). From symmetry, the field strength at the midpoint between the coils will be twice the value from the single coil:

$$B\left(\frac{R}{2}\right) = 2B_1\left(\frac{R}{2}\right) = \frac{2\mu_0 nIR^2}{2\left(R^2 + \left(\frac{R}{2}\right)^2\right)^{3/2}}$$

which simplifies to

$$B\left(\frac{R}{2}\right) = \left(\frac{4}{5}\right)^{\frac{3}{2}} \frac{\mu_0 nI}{R}$$

What makes Helmholtz coils desirable is the uniform magnetic field they produce in their center. However, changing the spacing between the coils will yield a non-uniform magnetic field. For non-uniform magnetic fields, the math becomes more complicated, involving the use of Bessel functions.

2.7 Percent Dose-Depth Curve and Calculating Dose Rate

It is worth briefly mentioning the percent dose-depth curve and how to calculate the dose rate for an electron beam. Figure 2.9 displays what is known as the percent dose-depth curve for electrons (PDD). The CSDA range mentioned in section 2.3 represents the mean path length along the electron's trajectory, and not the penetration depth in a specific

direction. There are two main concepts of range for electron beams: the maximum range and the practical range.

Maximum range, R_{max} (which can be *cm* or g/cm^2) is defined as the depth at which extrapolation of the tail of the central axis depth dose curve meets the bremsstrahlung background (see Figure 2.9) (Strydom et. al. 2005). It is the largest depth the electron will penetrate in an absorbing medium. The maximum range does not give a well-defined measurement point.

The practical range, R_p (*cm* or g/cm^2) is defined as the depth at which the tangent plotted through the steepest section of the electron depth dose curve intersects with the extrapolation line of the background due to bremsstrahlung (see Figure 2.9) (Strydom et. al. 2005).

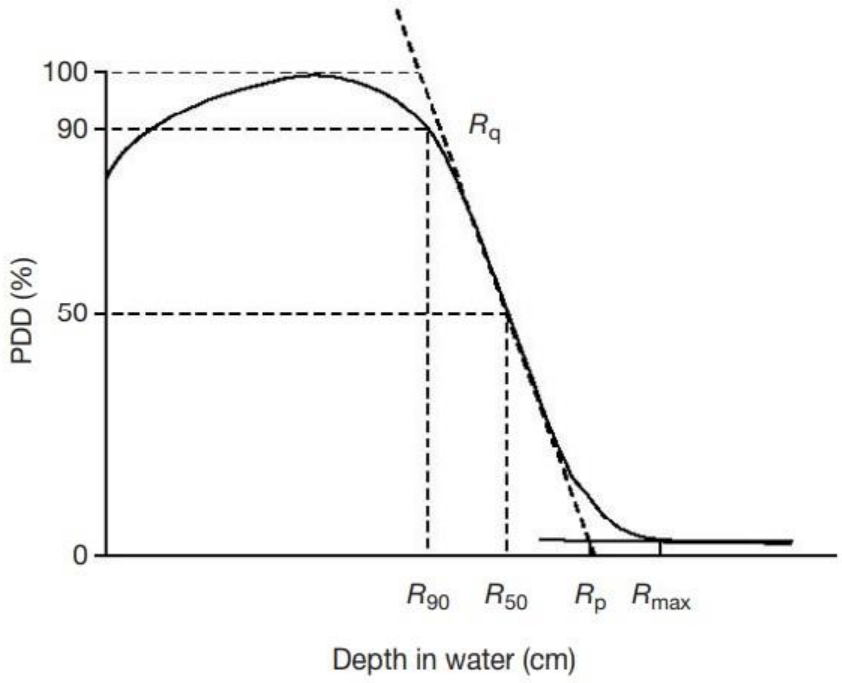

Figure 2.9: Typical electron beam PDD curve illustrating the definition of R_q, R_p, R_{max}, R_{50}, and R_{90}, from Strydom et. al.

R_{90} and R_{50} are the depths on Figure 2.9 in which the PDDs beyond the electron range for a given energy attain values of 90% and 50%, respectively. R_q is the depth where the tangent through the dose inflection point intersects the maximum dose level (Strydom et. al. 2005). These values constitute the parameters for electron depth dose as a function of energy. Such parameters should be known for an electron beam before it is used in clinical applications.

In a rather straightforward method, it is possible to calculate the theoretical radiation dose from an electron beam of specific energy incident on the surface of a known absorber medium. Taking data from the NIST-ESTAR database for a 200 *keV* electron and 1 *nA* of current through water. Assume a cylinder of water with radius (r) of 4 *mm* and length (L) of 5 *mm*. Applying some known values:

$$1\ eV = 1.6 \times 10^{-19}\ J$$

$$1\ A = 6.25 \times 10^{18}\ \ electrons/_{s}$$

$$Volume\ of\ cylinder = \pi r^2 L$$

$$Density\ of\ water \sim 1\ {}^{g}/_{cm^3}$$

$$Dose\ Rate: 1\ Gy = 1\ {}^{J}/_{kg}$$

Energy in terms of $J/electron$:

$$200 \times 10^3\ eV * 1.6 \times 10^{-19}\ {}^{J}/_{electron} = 3.2 \times 10^{14}\ {}^{J}/_{electron}$$

Number of electrons per second in 1 *nA*:

$$1\ nA = 6.25 \times 10^{9}\ {electrons}/{s}$$

Volume of the cylinder:

$$Volume = \pi(0.2\ cm)^2(0.05\ cm) = 6.3 \times 10^{-3}\ cm^3$$

Mass of the sample (water):

$$1\ {g}/{cm^3} * 6.3 \times 10^{-3} cm^3 = 6.3 \times 10^{-3} g$$

Power in ${J}/{s}$:

$$6.25 \times 10^{9}\ {electrons}/{s} * 3.2 \times 10^{14}\ {J}/{electron} = 2.0 \times 10^{-4}\ {J}/{s}$$

Giving a calculated dose rate (D):

$$1\ Gy = 1\ {J}/{kg}$$

$$D = \frac{Power}{Mass} = \frac{2.0 \times 10^{-4}\ {J}/{s}}{6.3 \times 10^{-6}\ kg} = 32\ {Gy}/{s}$$

$$\therefore D = 32\ {Gy}/{s} = 3200\ {Rad}/{s}$$

Since $1\ Gy = 100\ Rad$. This yields a large radiation dose distributed over a small volume. Gray (*Gy*) is a derived unit of absorbed ionizing radiation dose, and *Rad* (radiation absorbed dose), reflects the amount of energy that radioactive sources deposit in materials they pass through. In applications, calculated dose rate would ideally match measured dose rate.

Chapter Three

Experiments and Results

3.1 Materials and Design

Figure 3.1 is a diagram of the general experimental setup. The pressure within the vacuum chamber is maintained at ~10^{-6} *torr*. Pressure within the RN-400 Van de Graaff particle accelerator is kept at around 100 *psig* with a mixture of nitrogen, carbon-dioxide, and sulfur-hexafluoride. The exit window of the accelerator is located on the vacuum chamber. The exit window of the vacuum chamber is fitted with a thin aluminum foil. This foil is used to amplify the number of scattering events. Aligned head-on with the vacuum chamber, separated by a distance which will vary, is a cylindrical Geiger-Mueller (G-M) tube.

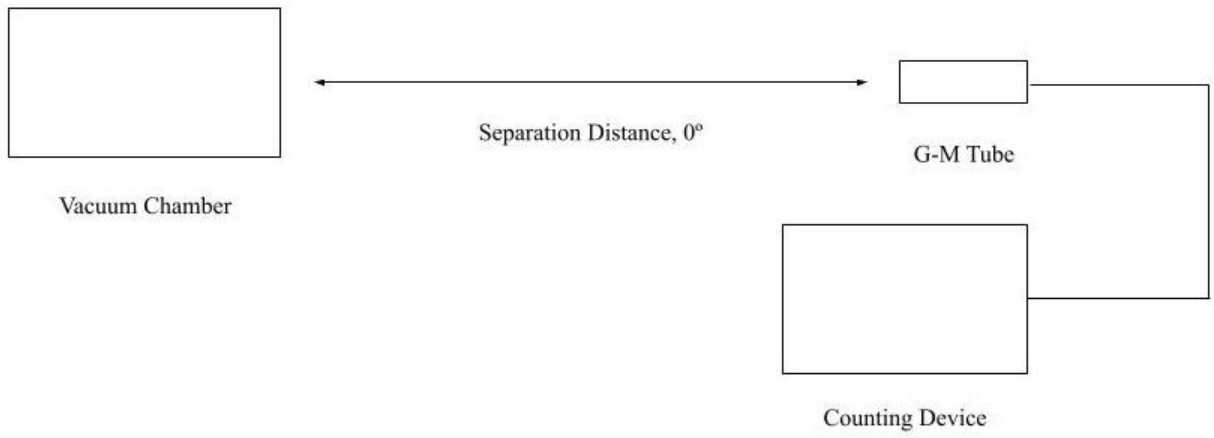

Figure 3.1: Schematic of general experimental setup

Affixed a few centimeters from the front of the G-M tube (detector) is a ^{65}Zn radioactive source. The purpose of this source is to provide a reference background count

for all measurements. The detector is wired to a power supply and maintained at a potential of +800 *V*. From section 2.4, this potential is selected for gas multiplication to occur within the tube. The detector is also connected to a pulse inverter, which will convert a negative tube signal into a positive pulse in the input connection of the counting device. Pulse inversion is necessary because the Geiger counter output is a negative pulse, and the Ortec Timer and Counter device requires a positive pulse at its positive input terminal. The timer on the counting device is set to measure counts for ten seconds.

The detector will occasionally be displaced at an angle relative to the head-on positioning with the vacuum chamber. These displacements will always be to the right, viewed from vacuum chamber to detector. Radiation (*Rad*) will be measured, but this reading is simply used to determine if a beam has been produced or not. A reading of 0 Rad would correspond to no beam being produced. Occasional electrical discharges ("sparks") within the accelerator vessel result in unused measurements since they will throw off the count rate. These "sparks" are due to a multitude of factors. The uncertainty in the GVM readings is given in the literature to be +/- 5 *keV*. The following sections in chapter three cover a series of experiments in the order in which they were conducted.

3.2 Verification of Electron Production Pt. 1

The RN-400 Van de Graaff particle accelerator was originally designed to produce a beam of positive ions. Previous students worked on reversing the polarity of the accelerator, so instead of producing positive ions, the accelerator would produce a beam of electrons. The students demonstrated they successfully reversed the polarity of the

accelerator, but never verified whether the accelerator was indeed producing an electrons beam. Generating voltmeter (GVM) recordings are not to be taken as entirely accurate due to the age of the control panel. The accelerator has been previously calibrated, finding a column current of 24.1 μA corresponds to kinetic energy of 340 *keV*. Column current readings are used to calculate the calibrated energy.

In section 2.3 it was stated that if one knows the CSDA range for an electron in a specific medium, and the density of the medium, the distance the electron will travel before coming to rest can be calculated.

From

$$x = \frac{R_{CSDA}}{\rho}$$

and looking up the CSDA range table for electrons in dry air (density of 0.001225 g/cm^3), the travel distance is calculated for various energies in Table 3.1.

Kinetic Energy (keV)	CSDA Range (g/cm^2)	Distance (cm)
200	0.05082	41.5
250	0.07213	58.9
300	0.09528	77.8
350	0.11990	97.9
400	0.14560	118.9

Table 3.2: CSDA Range and calculated travel distance for electrons in dry air

The detector is placed head-on with the vacuum chamber (0°). Background counts are measured to be approximately 4700 *counts/10s*. The detector is set at distances of 100

cm, 80 *cm*, 60 *cm*, 40 *cm*, 20 *cm*, and 15 *cm*. Column current is maintained to be as constant as possible. Calibrated energy is calculated from the column current. Two measurements are taken at each distance.

Table 3.2 displays the collected data. Any counts beneath background means the detector has become saturated, initiating continuous dead time. Data in Table 3.2 shows the detector is in dead time at 60 *cm*, and not in dead time at 80 *cm*, suggesting the travel distance of the accelerator beam to be somewhere in-between those distances. The calibrated energies from distance 60 *cm* and 80 *cm* are 279 *keV* and 272 *keV*, respectively.

θ (°)	Distance (cm)	GVM (keV)	Column Current (μA)	Calibrated Energy (keV)	Rad. (mR/hr.)	Counts/10s
0	100	205	19.5	275	14.3	9375
						10376
0	80	205	19.3	272	10.8	10864
						10863
0	60	205	19.8	279	13.3	236
						227
0	40	205	21.1	298	14.0	227
						259
0	20	205	20.3	286	13.6	155
						133
0	15	205	19.5	275	17.0	275
						215

Table 3.3: Counts/10s at varying distances

According to Table 3.1 and Table 3.2, the calibrated energies suggest the travel distance of the particles to be greater than 60 *cm*, and less than 77.8 *cm*, providing strong initial support for the production of electrons. Recordings in the GVM column of Table 3.2

demonstrate why readings from the GVM are not to be taken as the true energy. As the meter remains on 205 *keV* throughout this experiment, the column current varies.

3.3 Placement of Copper Absorbers

Applying the same method from section 3.2 for electrons in air, travel distance for electrons in a copper absorber (density of 8.96 g/cm^3) may also be calculated (Table 3.3). Keeping the same experimental setup as is described in section 3.2, with the same background counts, a copper absorber with a thickness of 3 *mm* is placed in front of the detector window. Another 3 *mm* thick copper absorber will then be added, giving a total thickness of 6 *mm*. While density effect parameter is included in Table 3.3, it is not necessary to account for it in this experimental setup.

Kinetic Energy (keV)	CSDA Range (g/cm^2)	Distance (cm)	Density Effect Parameter
200	0.06807	0.007597	0.08595
250	0.09603	0.010718	0.12360
300	0.12630	0.014096	0.16040
350	0.15840	0.017679	0.19580
400	0.19180	0.021406	0.23020

Table 3.4: CSDA Range and calculated distance for electrons in copper

According to the Table 3.3, a 400 *keV* electron will only travel ~0.021 *cm* within a copper absorber, so a single 3 *mm* copper absorber should be more than enough to block the detector and prevent dead time events from occurring. The detector is placed head-on

with the vacuum chamber at distances 20 *cm*, 40 *cm*, 60 *cm*, and 80 *cm*. At 80 *cm*, the detector is then displaced from the vacuum chamber at angles 30° and 90°. With the thickness of a single copper absorber being well beyond the predicted travel distance at the maximum kinetic energy that the accelerator can produce, readings are only recorded from the GVM, maintained at a constant 230 *keV*. Therefore, column current and calibrated energy are not recorded here.

θ (°)	**Distance (cm)**	**Counts/10s**		
		No Absorbers	**One Absorber (3mm)**	**Two Absorbers (6mm)**
0	20	155	13361	14529
0	40	302	16842	15095
0	60	369	11754	11746
0	80	13302	9305	8795
30	80	12486	8250	8559
90	80	9872	8793	-

Table 3.5: Count rate recordings of copper absorber experiment

Measurements in the “No absorbers” column of Table 3.4 is consistent with data from Table 3.2. When a single 3 *mm* copper absorber is added in front of the detector window the count rate rises considerably compared to when there is no absorber for distances of 20 *cm*, 40 *cm*, and 60 *cm*. By extension, similar results are observed with the addition of the second copper absorber. The data shows a single 3 *mm* copper absorber is more than enough to shield the detector from experiencing continuous dead time.

In both absorber cases, the significant rise in the count rate at distances 20 *cm* to 60 *cm* is due to the copper absorbers not perfectly covering the detector window. The

absorbers are rectangular in shape while the detector window is circular. Also, due to the sensitivity of the detector window, the copper absorbers are not allowed to be fixed to the device directly without risking damage. Due to these constraints, the copper absorbers are only preventing the detector from becoming saturated and initiating continuous dead time. For two absorbers at 80 *cm* and 90°, no measurement is taken since data leading up to that point is consistent with expectation.

At 80 *cm*, the placement of the detector at angle 30° for all three cases yields an interesting observation. There is a drop in the count rate for all cases at that angle in comparison to the 0° recordings. This suggests that there may be an angular distribution in the count rate. Further experimentation will be conducted to explore this possibility.

3.4 Verification of Electron Production Pt. 2

Results from section 3.2 indicate the accelerator may be producing a beam of electrons. A more carefully designed experiment is necessary to investigate this potential further. Using a similar method from section 3.2, and selecting distances 70 *cm*, 80 *cm*, and 90 *cm*, the distances will remain fixed while the column current is varied via the GVM control knob, corresponding to an increase in the calibrated energy. A single ten second count is taken at each increasing column current measurement. Background count is measured to be approximately 5800 *counts/10s*. Any count measurement at or around background will suggest the start of continuous dead time.

At a distance of 70 *cm*, the GVM control knob is turned so the column current steadily increases, thus increasing the calibrated energy. Measurements are taken when the

column current remains steady in order to obtain the most accurate data. A calibrated energy of 271 *keV* yields 14,551 *counts/10s*, well above background. When the calibrated energy is increased to 289 *keV* the count rate drops to 4,535 *counts/10s*, slightly below background, displaying the beginning signs of continuous dead time in the counting device. Increasing the calibrated energy to 305 *keV* yields a count rate of 263 *counts/10s*. The detector is now experiencing too many ionization events internally, and continuous dead time has taken over. The range data in Table 3.2 says that a 300 *keV* electron will travel 77.8 *cm*. Based on that data, for 305 *keV*, a reduced count rate is to be expected. Count rates at 70 *cm* for increasing calibrated energy demonstrate a clear transition from a high count, to one which is close to background, to one which is experiencing continuous dead time, at energies of 271 *keV*, 289 *keV*, and 305 *keV*, respectively.

Distance (cm)	GVM (keV)	Column Current (μA)	Calibrated Energy (keV)	Rad. (mR/hr.)	Counts/10s
70	220	19.2	271	18.0	14551
70	235	20.5	289	15.0	4535
70	240	22.0	310	23.0	257
70	240	21.6	305	17.0	263
70	250	22.3	315	16.0	89
70	260	23.6	333	21.0	38
70	270	24.0	339	23.0	27
80	215	19.0	268	11.0	12359
80	240	21.0	296	16.0	12421
80	270	23.5	332	20.0	474
80	290	26.0	367	25.0	24
80	240	21.0	296	14.0	15979
90	225	20.0	282	12.0	11133
90	240	21.0	296	14.0	12054
90	260	25.0	353	21.0	6269
90	280	25.7	363	22.0	1440
90	295	26.3	371	23.0	496
90	300	27.1	382	24.0	155

Table 3.6: Count rate for distances 70cm, 80cm, and 90cm in descending order of GVM measurements

Five count measurements at a distance of 80 *cm* are measured, with two measurements at 296 *keV*. Count rates at 268 *keV* (12,359 *counts/10s*) and 296 *keV* (12,421 & 12,421 *counts/10s*) may be considered equivalent. Count rates at 332 *keV* (474 *counts/10s*) and 367 *keV* (24 *counts/10s*) may also be considered equivalent. Referring to Table 3.2, energies between 300 *keV* and 350 *keV* correspond to ranges of 77.8 *cm* to 97.9 *cm*. For the distance of 80 *cm*, a clear shift toward continuous dead time in the detector happens between energies 296 *keV* and 332 *keV*. Count measurements for 80 *cm* strongly correspond to expectation from the CSDA range table.

At 90 *cm*, six count measurements are recorded. Beginning with a calibrated energy of 282 *keV*, the energy is increased upward to 382 *keV*. From Table 3.2, a distance of 90 *cm* should require an energy greater than 300 *keV* but less than 350 *keV*. Three distinct measurements stand out most. An energy of 296 *keV* yields a count rate of 12,054 *counts/10s*. An energy of 353 *keV* yields a count rate of 6,269 *counts/10s*. And an energy of 363 *keV* yields a count rate of 1,440 *counts/10s*. These three energies show the transitional period Table 3.2 would suggest. A high count rate around 300 *keV*, a shift toward continuous dead time events around 350 *keV*, and continuous dead time for energies well above 350 *keV*.

Measurements recorded at all three distances strongly suggest the particles being produced by the accelerator are indeed electrons. At a set distance, when the energy is lower than what is required to reach that distance, a high count rate is measured. When the energy is higher than what is required to reach that distance, continuous dead time takes over and a low count rate is measured.

3.5 Count Rate as a Function of Energy

Data collected in the copper absorber experiment suggests the possibility of angular distribution. The count rate at 80 *cm* oriented 0° has a count rate of 13,302 *counts/10s*. When the angle was increased to 30° the count rate dropped to 12,486 *counts/10s*, which is not a significant drop compared to the 0° orientation. However, when the angle was increased further, to 90°, the count rate dropped to 9,872 *counts/10s*, a considerable decrease. The question now becomes, at a given distance and angle relative to the exit window of the vacuum chamber, what happens to the count rate as the energy increases?

For this experiment, distances of 80 *cm*, 90 *cm*, and 100 *cm* are chosen, as well as angles of 0° (reference angle), 45°, and 75°. At distances 90 *cm* and 100 *cm*, the narrowness of the lab room does not allow for the detector to be placed at angles greater than 75°. For each angle, the detector is placed at 80 *cm*, 90 *cm*, then 100 *cm*, and counts are measured as energy increases. This process is then repeated for the two angles. Again, ten second counts are used. This time, column current (used to give calibrated energy) from the GVM control knob will be increased slowly, giving incremental increases to the calibrated energy. The radioactive source attached to the detector is changed to Thallium-204 and is used as the new background reference. The background count is measured to be approximately 3,000 *counts/10s*.

Table 3.7 shows the data collected for the detector oriented at 0° and Figure 3.2 is the corresponding graph of counts (per 10s) as a function of energy, for the distances of 80 *cm*, 90 *cm*, and 100 *cm*. Some distances have less measurements due to stability issues with the accelerator. Uncertainty in column current readings is difficult to account for since all

measurements are eyeball estimates from watching the meter for ten seconds and column current sporadically changing each time the energy is increased. For all three distances, a similar trend is observed. There is a clear buildup region for 90 *cm* and 100 *cm* at energies leading to their CSDA range, followed by quick drop in the counts as the energy goes beyond their CSDA range. The 80 *cm* distance appears to be in the beginning stage of continuous dead time from the beginning.

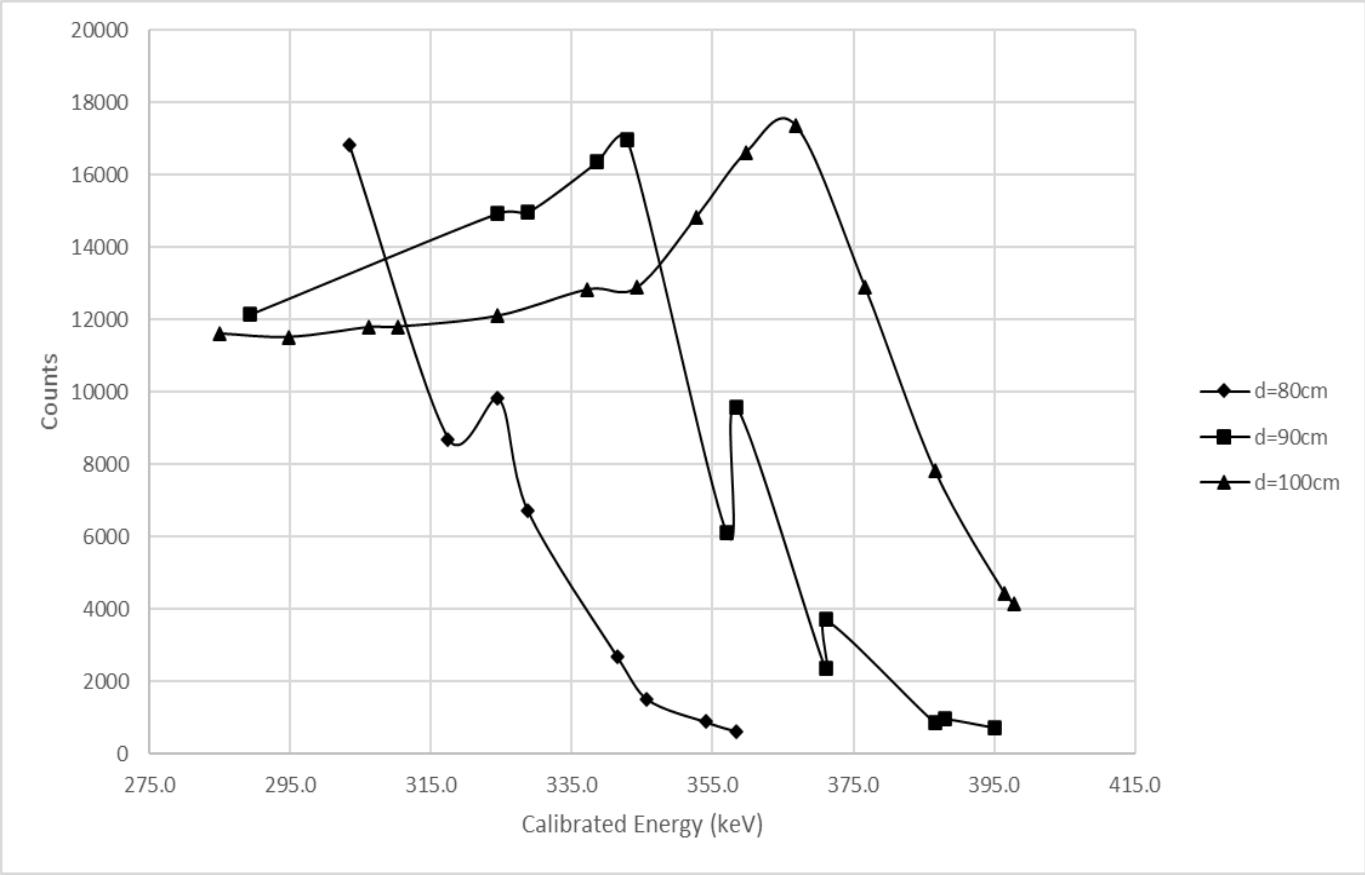

Figure 3.2: Counts as a function of energy for distances 80cm, 90cm, 100cm at 0°

Θ (°)	Distance (cm)	GVM (keV)	Column Current (μA)	Radiation (mR/hr.)	Counts/10s	Calibrated Energy (keV)
0	80	250	21.5	15.0	16822	303
0	80	260	22.5	16.0	8705	317
0	80	265	23.0	16.0	9828	324
0	80	270	23.3	17.0	6716	329
0	80	275	24.2	18.0	2691	341
0	80	280	24.5	19.0	1514	346
0	80	285	25.1	19.0	880	354
0	80	290	25.4	21.0	625	358
0	90	200	20.5	19.0	12151	289
0	90	260	23.0	22.0	14954	324
0	90	265	23.3	18.0	14982	329
0	90	270	24.0	22.0	16372	339
0	90	275	24.3	19.0	16991	343
0	90	280	25.3	25.5	6125	357
0	90	285	25.4	20.0	9593	358
0	90	290	26.3	30.0	2346	371
0	90	295	26.3	21.0	3705	371
0	90	300	27.4	36.0	861	387
0	90	305	27.5	25.0	969	388
0	90	310	28.0	31.0	730	395
0	100	230	20.2	20.0	11618	285
0	100	235	20.9	18.0	11525	295
0	100	240	21.7	20.0	11794	306
0	100	245	22.0	20.0	11809	310
0	100	255	23.0	22.5	12109	324
0	100	265	23.9	25.0	12835	337
0	100	270	24.4	26.0	12888	344
0	100	275	25.0	28.0	14837	353
0	100	280	25.5	26.0	16623	360
0	100	290	26.0	27.5	17373	367
0	100	295	26.7	23.0	12891	377
0	100	305	27.4	30.0	7843	387
0	100	310	28.1	31.0	4449	396
0	100	315	28.2	29.0	4147	398

Table 3.7: Counts at distances 80cm, 90cm, and 100cm for increasing calibrated energies with detector at 0°

The detector is then oriented to 45° and the process is repeated. Table 3.8 and Figure 3.3 display the collected data. A similar trend to the 0° orientation is apparent. This time the distance of 80 *cm* shows a clear buildup region. Comparing the peaks of the distances in Figure 3.2 with Figure 3.3 shows that when the detector is oriented at an angle, the amount of energy required to initiate continuous dead time increases. This is the case for

all three distances recorded. For the distance of 100 *cm*, the amount of energy required to reach continuous dead time is beyond the amount of energy the accelerator is capable of reaching, which is 400 *keV*. The accelerator begins to become more unstable beyond 375 *keV*, leading to more electrical discharges internally, throwing off count measurements. Measurements are taken when everything is stable, excluding small variations in the column current.

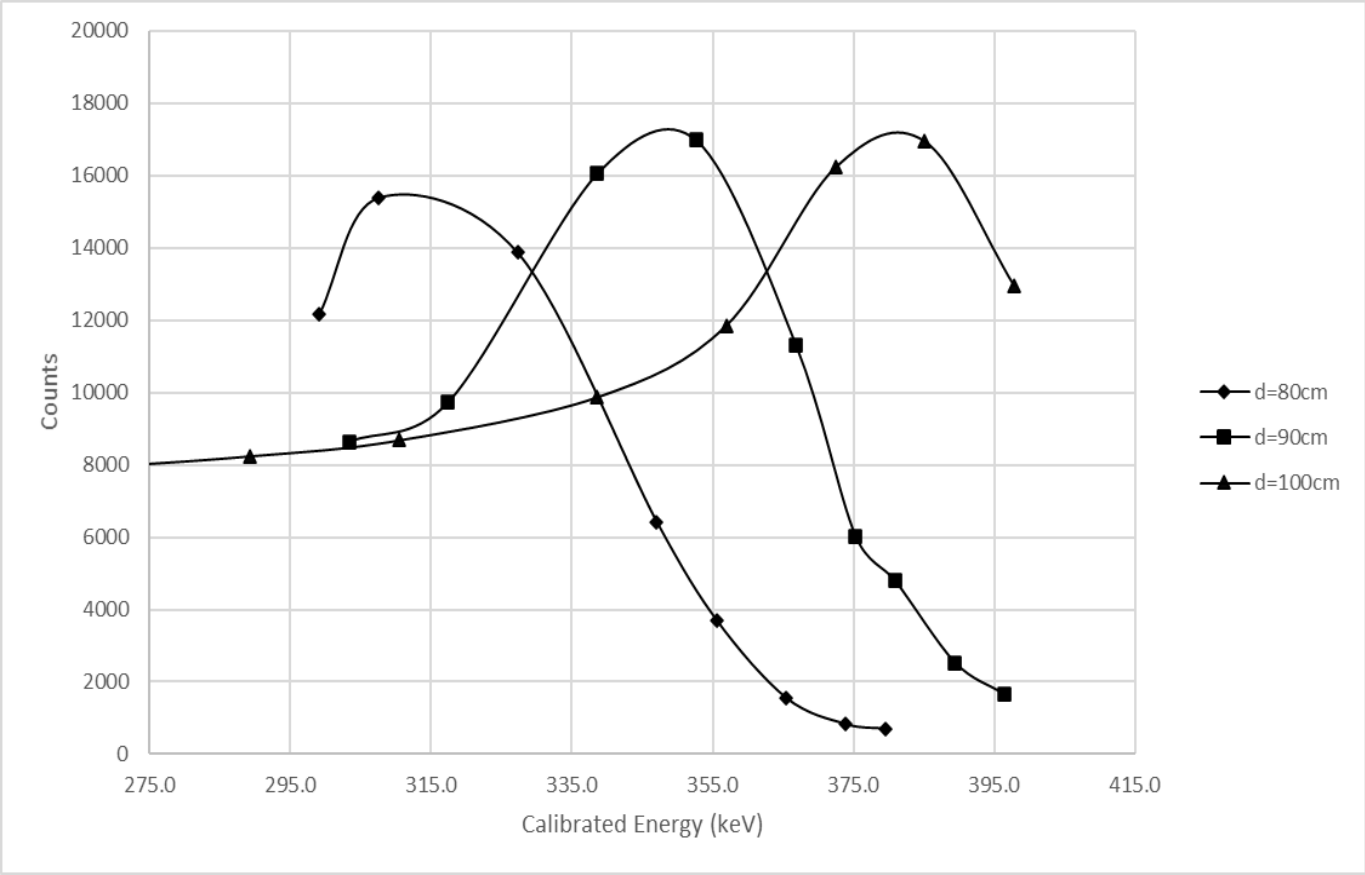

Figure 3.3: Counts as a function of energy for distances 80cm, 90cm, 100cm at 45°

Θ (°)	Distance (cm)	GVM (keV)	Column Current (μA)	Radiation (mR/hr.)	Counts/10s	Calibrated Energy (keV)
45	80	245	21.2	21.0	12158	299
45	80	255	21.8	27.0	15399	308
45	80	260	23.2	22.0	13876	327
45	80	270	24.6	25.0	6425	347
45	80	275	25.2	26.0	3709	356
45	80	285	25.9	27.0	1558	365
45	80	290	26.5	29.0	831	374
45	80	305	26.9	27.0	702	380
45	90	245	21.5	16.0	8642	303
45	90	255	22.5	17.0	9748	317
45	90	270	24.0	22.0	16061	339
45	90	275	25.0	23.0	16975	353
45	90	285	26.0	24.0	11317	367
45	90	295	26.6	29.0	6029	375
45	90	300	27.0	29.0	4789	381
45	90	305	27.6	30.0	2534	389
45	90	310	28.1	31.0	1646	396
45	100	215	18.7	16.0	7891	264
45	100	235	20.5	17.0	8246	289
45	100	245	22.0	18.0	8684	310
45	100	255	24.0	24.0	9876	339
45	100	280	25.3	27.0	11853	357
45	100	290	26.4	29.0	16225	372
45	100	300	27.3	35.0	16949	385
45	100	305	28.2	36.0	12964	398

Table 3.8: Counts at distances 80cm, 90cm, and 100cm for increasing calibrated energies with detector at 45°

The detector is then oriented again, this time at 75°. Another trend similar to 0° and 45°, is shown in Figure 3.4. At 80 *cm*, a more apparent buildup region is shown. The required energy to initiate continuous dead time at a distance 90 *cm* has now become unreachable for the accelerator. For the distance of 100 *cm*, only a buildup region is shown, continuing from the 45° orientation, the accelerator is not capable of reaching the energy required to initiate continuous dead time. Following from the previous graphs, the required energy to initiate continuous dead time has increased for all three distances. Also, the peak

of each graph becomes broader as the angle increases. All three graphs show that as the detector is positioned at an angle, the energy required to initiate continuous dead time within the detector increases. Results also further verify the production of electrons since data is consistent with CSDA range table values.

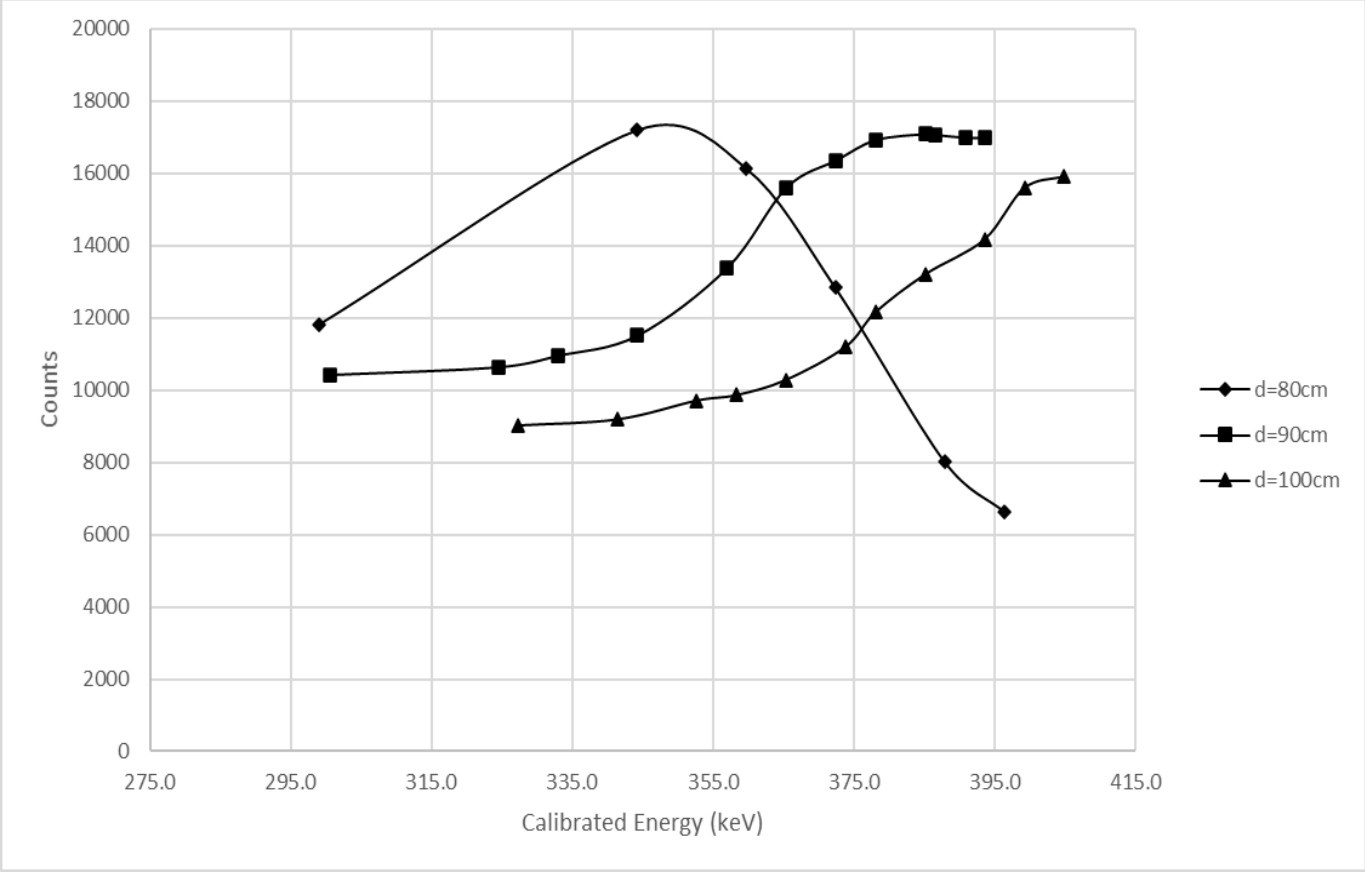

Figure 3.4: Counts as a function of energy for distances 80cm, 90cm, 100cm at 75°

Θ (°)	Distance (cm)	GVM (keV)	Column Current (μA)	Radiation (mR/hr.)	Counts/10s	Calibrated Energy (keV)
75	80	255	21.2	16.0	11827	299
75	80	275	24.4	19.0	17205	344
75	80	285	25.5	23.5	16146	360
75	80	295	26.4	25.6	12833	372
75	80	305	27.5	31.5	8018	388
75	80	310	28.1	32.0	6638	396
75	90	245	21.3	21.0	10423	300
75	90	255	23.0	22.0	10640	324
75	90	260	23.6	23.0	10957	333
75	90	265	24.4	24.0	11517	344
75	90	275	25.3	26.0	13380	357
75	90	285	25.9	28.0	15611	365
75	90	290	26.4	29.0	16367	372
75	90	295	26.8	30.0	16931	378
75	90	300	27.3	31.0	17097	385
75	90	300	27.4	27.0	17072	387
75	90	305	27.7	28.0	16997	391
75	90	310	27.9	28.0	16989	394
75	100	265	23.2	19.0	9025	327
75	100	270	24.2	21.0	9193	341
75	100	280	25.0	22.0	9714	353
75	100	285	25.4	23.0	9866	358
75	100	290	25.9	23.0	10287	365
75	100	295	26.5	25.0	11203	374
75	100	300	26.8	27.0	12154	378
75	100	305	27.3	28.0	13203	385
75	100	305	27.9	29.0	14174	394
75	100	310	28.3	31.0	15592	399
75	100	315	28.7	31.0	15918	405

Table 3.9: Counts at distances 80cm, 90cm, and 100cm for increasing calibrated energies with detector at 75°

3.6 Electron Beam through a Pair of Helmholtz Coils

With the production of electrons verified, attention is now shifted toward potential applications. A beam of electrons can be bent in the presence of a sufficiently strong magnetic field. Helmholtz coils allow for a uniform magnetic field which can be controlled from outside the accelerator room by varying the current through the coils with a standard power supply. If it can be demonstrated that the Helmholtz coils can bend the electron beam it will be a useful tool for future student-led research projects.

For this experiment, a Pasco Scientific Helmholtz coil apparatus is used. The coils have radius of 10.5 *cm*, with 200 *turns* of copper wire, and a resistance of 1.2 *k*Ω. The maximum current allowed through the coils is limited to 2 *A*. The base holding the coils allows for a separation distance to vary between 10-20 *cm*. The coils will be placed at a determined distance and calibrated to provide a magnetic field which will curve the electron beam to the right when viewed from the vacuum chamber toward the detector (see Figure 3.5). The detector will be placed at angles relative to the exit window (labeled "source" on Figure 3.5).

Several variables require being accounted for in this experiment. First, electrons will lose their energy as they fly through the air in the room. An electron with initial energy of 400 *keV*, after traveling some distance, will have a lower energy value. This means the electrons will have a new energy by the time they reach the Helmholtz coils after leaving the accelerator. To account for this, data collected from the NIST-ESTAR database is used to calculate the energy loss as a function of distance. This is achieved by starting with the maximum energy, 400 *keV* for this accelerator.

The difference in range for 400 *keV* electron is taken to be 0 *cm* since it is considered the initial energy. Then using the preceding energy from the database, 350 *keV*, the range of this energy (97.9 *cm* in dry air) is subtracted from the range of the 400 *keV* electron (118.9 *cm* in dry air). This gives a difference of 21 *cm*. This value is now summed by the difference calculation of the 400 *keV* electron. Since the difference calculation at 400 *keV* (the initial energy) is 0 *cm*, the total would be the sum of 21 *cm* and 0 *cm*, therefore the total difference at 350 *keV* is 21 *cm*. So, this means that when a 400 *keV* electron travels 21 *cm*, it will lose 50 *keV*, making it a 350 *keV* electron at that point in dry air.

This process is then repeated until reaching the lowest possible energy the database has, 10 *keV*. This means if the initial energy of the electron beam is known, its energy loss as a function of distance can be accounted for (see Figure 3.6). Knowing the energy loss as a function of distance will allow for proper placement of all equipment.

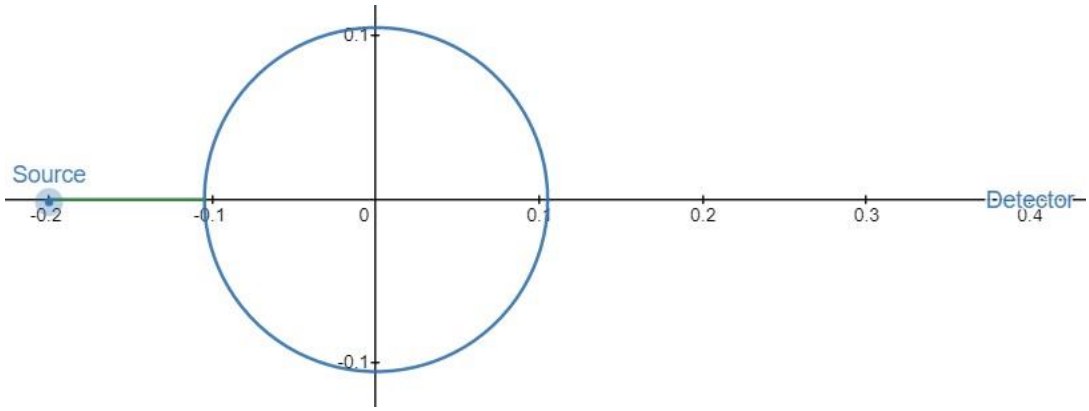

Figure 3.5: Desmos generated diagram of the Helmholtz coils setup. Values listed are in meters. These values can be adjusted within Desmos to fit experimental needs.

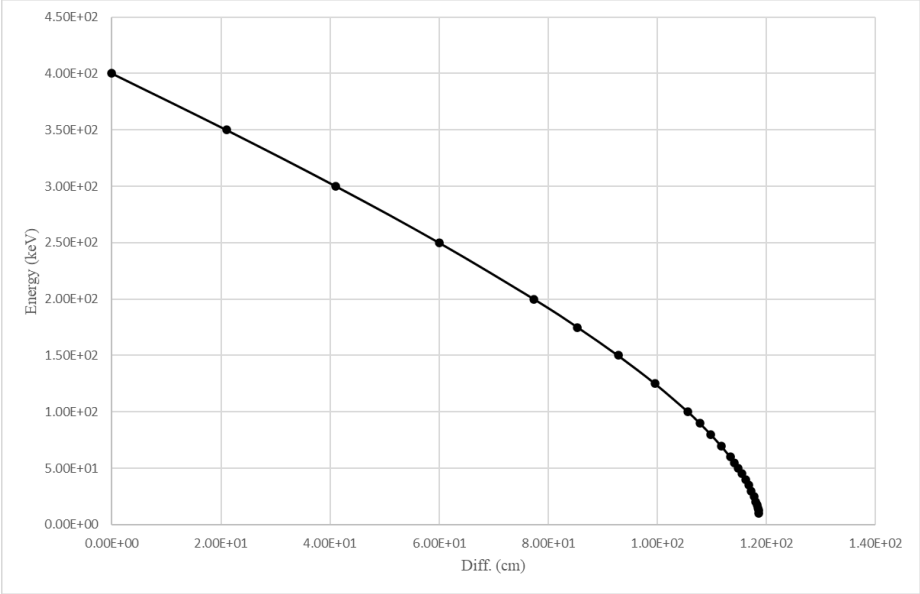

Figure 3.6: Energy loss as a function of distance for a 400keV electron in dry air

The online graphing website Desmos is used for all calculations. Desmos gives the ability to create an interactive environment in which sliders for each variable allow for on-the-fly adjustments. Desmos is able to account for the energy, the energy loss through air, the current in the coils, the number of turns of wire, the strength of the magnetic field, the distance between the coils and the exit window (source), the distance between the coils and the detector, the distance between the source and the detector, the angle the detector will be placed, etc. Every variable which can be controlled is entered into Desmos with a slider feature, allowing to change the parameters of the experiment in real time. Figure 3.7 shows a snapshot of the main menu of the Desmos program.

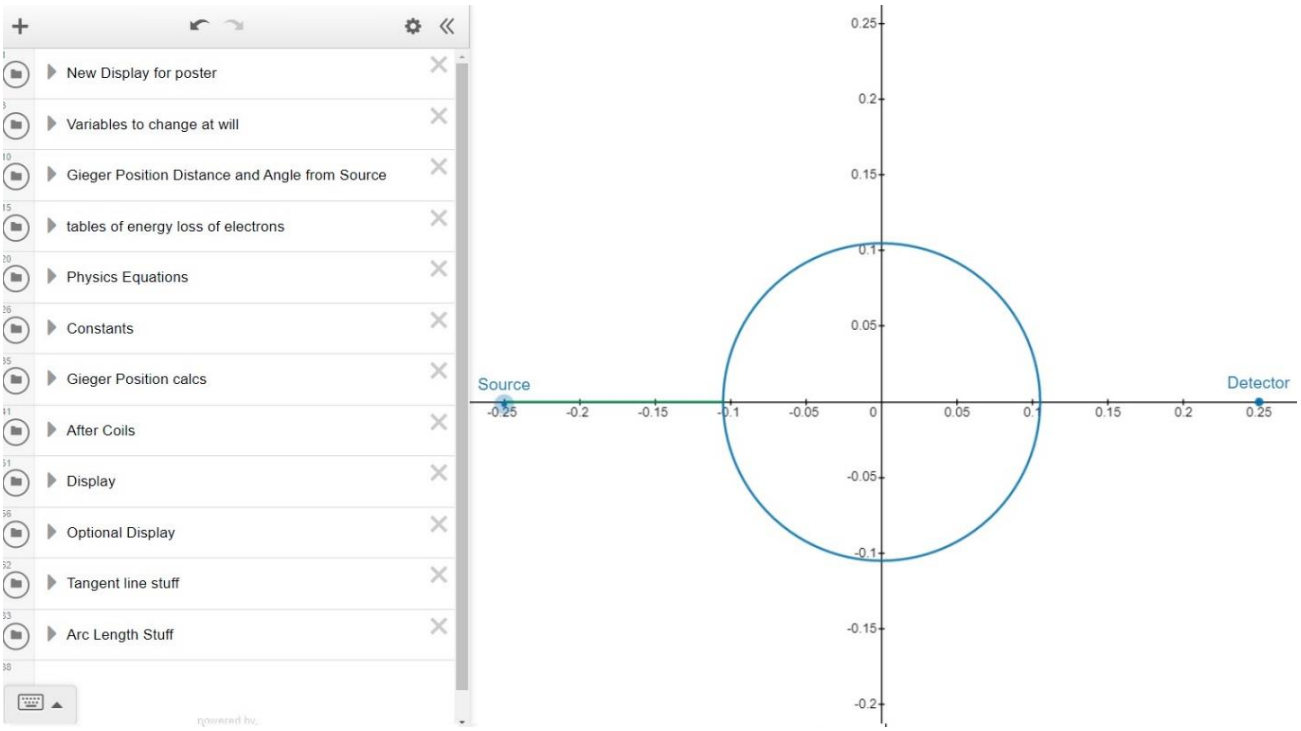

Figure 3.7: Snapshot of Desmos menu for experiment

The first experiment tests whether the beam can be deflected toward the detector. The Desmos program has not yet been completed for this experiment, and the experiments only goal is to verify if the beam can be deflected toward a detector. The detector is placed at an angle of 45° relative to the center of the coils. The distance from the source to the center of the coils is 30 *cm* and the distance from the center of the coils to the detector is 25 *cm*. Background is measured to be approximately 4150 *counts/10s*. The GVM control knob is set to minimum and any changes in column current will be the result of the accelerator not maintaining a stead column current itself. Coil current starts at 0.3 *A* and is then steadily increased by 0.1 *A* until reaching the limit of what the power supply would allow (1.245 *A*). PVC pipe is carefully fitted around the detector in the event a broad beam is produced from the accelerator. Results are shown in Table 3.10.

During the experiment the GVM control was never touched, and internal electrical discharges caused the column current to increase. This increase appeared to have negligible effects on the results. Due to the beam energy and proximity of the detector to the source, the detector began experiencing continuous dead time. However, increasing the coil current did yield a further decrease in the counts for measurements which had similar column currents. This suggests the beam is possibly bent toward the detector, but due to the small count rate, results are not conclusive.

Angle (°)	Coil Current (A)	Column Current (μA)	Calibrated Energy (keV)	Rad. (mR/hr.)	Counts/10s
45	0.300	18.5	261	10.0	2032
45	0.400	18.5	261	10.0	1140
45	0.500	18.5	261	10.0	924
45	0.600	19.3	272	10.0	874
45	0.700	19.3	272	10.0	893
45	0.800	19.3	272	10.0	792
45	0.900	19.3	272	10.0	415
45	1.000	19.5	275	10.0	312
45	1.100	19.5	275	10.0	403
45	1.200	19.5	275	10.0	257
45	1.245	19.5	275	10.0	317

Table 3.10: Count rate of electron beam through Helmholtz coils for increasing coil current at coil distance 30cm from source

Another experiment was conducted using the exact same approach as the previous. This time, careful attention was paid to maintain the column current (calibrated energy) as much as possible. The distance from the center of the coils to the detector window is 25 *cm* and the distance from the source to the center of the coils is 50 *cm*. The coils are moved further away from the source in order to prevent the detector from beginning the experiment experiencing prolonged dead time. Background is measured to be approximately 4,300 *counts/10s*. The current begins at 0.0 *A* and is increased in increments of 0.1 *A* until reaching 1.2 *A*. Figure 3.8 displays the results.

Angle (°)	Coil Current (A)	Column Current (μA)	Calibrated Energy (keV)	Rad. (mR/hr.)	Counts/10s
45	0.000	19.5	275	10.0	9062
45	0.100	19.5	275	10.0	8483
45	0.200	19.5	275	10.0	9166
45	0.300	19.5	275	10.0	9042
45	0.400	19.5	275	10.0	7362
45	0.500	19.5	275	10.0	7064
45	0.600	19.5	275	10.0	6599
45	0.700	19.5	275	10.0	7321
45	0.800	19.5	275	10.0	7170
45	0.900	19.5	275	10.0	6969
45	1.000	19.5	275	10.0	6913
45	1.100	19.5	275	10.0	7935
45	1.200	19.5	275	10.0	7669

Table 3.11: Count rate of electron beam through Helmholtz coils for increasing coil at coil distance 50cm from source

Results from moving the Helmholtz coils to 50 *cm* from the source shows similar results to the Helmholtz coils at 30 *cm*. The position of the detector and the coils is chosen so that the detector does not begin in a state of continuous dead time. Careful attention is paid to maintaining the calibrated energy to be consistent throughout. Measurements that vary greatly are dismissed, only keeping measurements where column current is steady throughout the ten second count. Between coil currents 0.0 *A* and 0.3 *A* the count rate is similar, with a small drop in counts at 0.1 *A*. There is no considerable change in the counts. From 0.4 *A* to 1.2 *A* the count rate decreases considerably but remains steady throughout the remainder of the experiment. Like the previous experiment, results suggest something is happening to the electron beam as it passes through the Helmholtz coils, but as to what exactly it might be, has not been determined conclusively.

A further dozen experiments are conducted, each returning inconclusive results. Work is undertaken to double the amount of turns in the Helmholtz coils, to 400 *turns*, and increasing the current through the coils to reach the maximum of 2 *A*. This is done to

increase the strength of the magnetic field thus enabling increased beam curvature which is necessary for higher electron energies. The higher the electron energy, the stronger the magnetic field must become to obtain the same radius of curvature in comparison to a lower electron energy. The doubling of the coils is accomplished by attaching another set of Pasco Scientific Helmholtz coils directly to the original setup.

Two major constraints prove difficult to overcome. First, the additional Helmholtz coils introduce a small gap between the pair of coils on the top, as well as the pair of coils on the bottom. While this gap may not seem significant, it is enough to create a non-uniform magnetic field at the midpoint between the top pair and bottom pair of coils. Also, the additional set of coils changes the separation distance between the top pair of coils and the bottom pair of coils, where the separation distance is no longer equivalent to the radius of the coils. This too, will cause a non-uniform magnetic field at the center of the pair of top and bottom coils. Future work will be required to investigate the uniformity of the magnetic field being produced by the setup.

While subsequent experiments returned inconclusive results, the data suggests the magnetic field is affecting the electron beam, but to what extent will require future investigation where all constraints are accounted for. Despite inconclusive data, development of a method for solving the energy loss as a function of distance in a given medium and the creation of the interactive Desmos program may prove to be useful tools for future experimentation. The energy loss as a function of distance also has an interactive Desmos program and can be programmed to change mediums which have data provided by the NIST-ESTAR database. Results also confirm a beam, specifically, is not being generated, but rather a large scattering of electron spraying into the room.

3.7 Radiation Safety Badge Experiment

To determine the radiation dose coming from the electron beam an experiment is designed to irradiate a radiation safety badge (Luxel+) provided by Landauer, Inc. (see Figure 3.8). These badges provide beta radiation monitoring with optically stimulated luminescence (OSL). Optically stimulated luminescence is a process in which a pre-irradiated material, when subjected to an appropriate optical stimulation, emits a light signal proportional to the absorbed dose (Pradhan et. al. 2008). The OSL radiation detector inside the Luxel+ dosimeter is a thin strip of specially formulated aluminum oxide (Al_2O_3) crystalline material. According to the Landauer website, during analysis, the aluminum oxide strip is stimulated with selected frequencies of laser light causing it to luminesce in proportion to the amount of radiation and the intensity of stimulation light. This badge monitors whole body radiation dose and is to be worn on the chest.

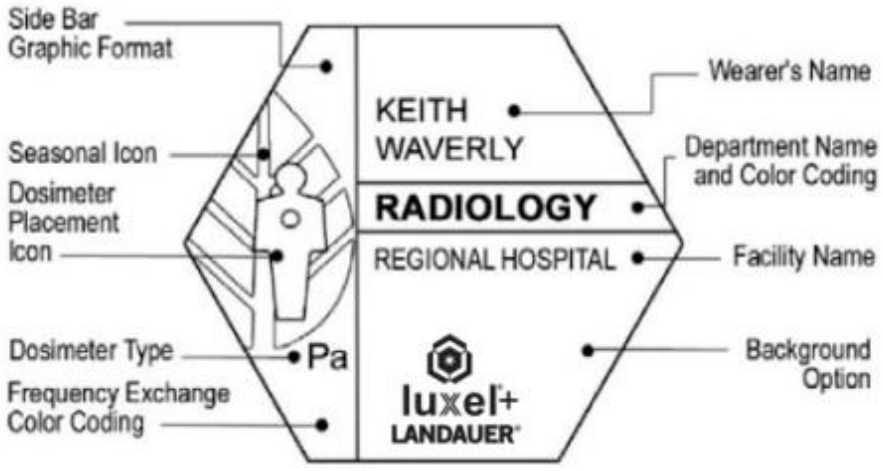

Figure 3.8: Basic design of radiation safety badge provided by Landauer (from their website)

The luminescence measured during analysis is applied to a dose algorithm which relies on the response ratios between different filter positions within the dosimeter to discriminate between beta, x-ray, and gamma radiations to determine exposure results. According to Landauer, beta exposures are reported only as a shallow dose equivalent.

First the accelerator is turned on and allowed to run until a stable beam is achieved. The accelerator is then shut off and the badge is placed facing the exit window of the vacuum chamber 8cm away. The accelerator is then turned on and measurements are taken every ten seconds for five minutes. An additional ammeter is attached to the experimental setup to measure the beam current (stray beam). The After the five minutes, the badge is then sent off to Landauer, Inc. for inspection. Landauer will then send a report back with the measurements from the badge. Data from the experiment is included in Table 3.12 and a reproduction of the results returned from Landauer is included in Table 3.13. *Rads* in Table 3.12 is measured in *millirad/hr*. (*mR*).

Time (s)	Stray Beam (nA)	Column Current (μA)	Rads (mR/hr.)
10	8.5	25.1	168
20	7.0	29.1	242
30	8.5	27.3	273
40	7.0	24.8	286
50	6.0	25.5	138
60	7.0	24.6	139
70	6.5	24.6	144
80	5.0	25.5	142
90	4.5	24.9	109
100	4.5	25.3	93
110	5.0	25.0	99
120	4.5	24.8	74
130	4.5	25.5	96
140	4.5	24.8	86
150	5.5	24.1	59
160	3.0	24.7	56
170	3.5	25.2	70
180	6.0	25.4	60
190	4.0	24.9	90
200	6.0	24.6	79
210	4.5	25.4	69
220	4.0	25.5	66
230	5.0	24.6	22
240	2.5	25.3	64
250	6.0	24.5	52
260	3.5	25.6	59
270	3.0	25.4	58
280	3.5	26.1	60
290	3.0	25.3	54
300	1.5	26.0	52

Table 3.12: Data collected for the radiation safety badge experiment

Default Override Levels (mrem)					
	Deep	**Lens**	**Shallow**	**Extremity**	**Fetal**
Wear Period	1000	3000	10000	10000	100
Year to Date	2500	7500	25000	25000	250
† Participant Override Level					

Table 3.13: Reproduction of the results returned from Landauer. Values of interest include Wear Period - Deep, and Wear Period – Shallow

During the experiment four electrical discharge events are noted, with a significant discharge at time 230 *sec*. This discharge affected the Rads measurement but seemed not to change the stray beam current or the column current. The ammeter measuring the stray

beam current is noted that the needle jumps two times during the internal discharge events. All of these can have a potential impact on the dose rate.

From the data returned by Landauer, there was an additional note which stated "Dosimeter has exceeded the reporting capabilities of 1,000 *rads*. Dosimeter reprocessed, second read agrees with reported dose." It is not entirely clear if Landauer is referring to Wear Period – Deep (WPD) or Wear Period – Shallow (WPS) in Table 3.13, therefore both values must be considered. The message indicates the badge ceased recording the dose rate once those values were exceeded, this gives a minimum dose rate range for consideration. WPD is measured at 1,000 *millirem* (*mrem*), and WPS is measured at 10,000 *mrem*. Since the badge is exposed to the electron beam for five minutes, these values become 200 *mrem/min* for WPD and 2,000 *mrem/min* for WPS.

One *rem* is the equivalent of one *rad*. (*R*), and one hundred rads is the equivalent of one *gray* (*Gy*). Therefore, based on the data provided by Landauer, a minimum dose rate range produced by the electron beam is between 2-20 *Gy/min*.

Chapter Four

Summary and Conclusion

Experiments verify the production of electrons from the RN-400 Van de Graaff particle accelerator using a novel method referred to as “kill the detector” through the utilization of continuous dead time in a G-M counter. At distances of 80 *cm*, 90 *cm*, and 100 *cm*, oriented at 0°, kinetic energies of 315±5 *keV*, 345±5 *keV*, and 360±5 *keV* are measured, respectively. At a distance of 100 *cm*, oriented at 45°, kinetic energies of 380±5 *keV* is measured, an increase from the 0° orientation. Thus demonstrating for a fixed distance, an increase in kinetic energy is required when the detector is oriented at an angle. Results are consistent with distance calculations using data for electrons in dry air obtained from the NIST-ESTAR database, given for an orientation at 0°, and in agreement with the energy loss as a function of distance Desmos program estimate.

Results from the Helmholtz coils experiments are inconclusive. Constraints involving equipment proved difficult to overcome as well as a large scattering of the electron beam. Several experiments demonstrate the generated magnetic field is slightly affecting the electron beam, but to what extent will require further, more careful, investigation. Despite the experimental woes, development of a method for calculating the energy loss as a function of distance and the creation of an interactive Desmos program for the Helmholtz coil experiment will be useful tools for future student-led research projects.

The radiation safety badge experiment provided a minimum range for the dose rate of the electron beam. The badge has a deep dose limit of 1,000 *R* and a shallow dose limit of 10,000 *R*. The attached message from the company claims the limit was exceeded, but

it was not clear which limit they were specifically referencing so both measurements must be considered. This implies five minutes of exposure to the beam energy at a distance of 8 *cm* from the exit window, delivered a minimum dose rate between 2-20 *Gy/min*, a sufficiently high dose of radiation. Since the limit of the radiation badge was exceeded in five minutes, another experiment was conducted exposing a radiation badge to beam energy for two minutes. Results of this experiment are still pending.

Despite the good and bad of the Helmholtz coils experiments, the goals of this study have been achieved. During the past year, undergraduate students performed a series of experiments using the results in this study. These experiments included irradiating fruit fly eggs, and irradiating cell assays. Other projects are already in the works to improve data collection, so measurements will no longer be eyeball estimates. This project includes a computer program to capture data from all accelerator display meters in real time. This will drastically improve future studies as well as their accuracy. The Helmholtz coils experiment showed great promise and the hope is that future work will be undertaken to improve the experimental setup as well as expand the Desmos program to include new features.

REFERENCES

"Stopping Power and Range Tables for Electrons." n.d. Physics.nist.gov. https://physics.nist.gov/cgi-bin/Star/e_table.pl.

Attix, Frank. 1986. *Introduction to Radiological Physics and Radiation Dosimetry*. Wiley-Interscience.

Berger, Martin J, Stephen M Seltzer, U.S Office, United States., and United States. 1983. *Stopping Powers and Ranges of Electrons and Positrons*. Washington, Dc: U.S. Dept. Of Commerce, National Bureau Of Standards ; Springfield, Va.

Bygrave, William D, Paul A Treado, and James M Lambert. 1970. *Accelerator Nuclear Physics : Fundamental Experiments with a van de Graaff Accelerator*. Burlington, Mass.: High Voltage Engineering Corp.

Christensen, Doran M., Carol J. Iddins, and Stephen L. Sugarman. 2014. "Ionizing Radiation Injuries and Illnesses." *Emergency Medicine Clinics of North America* 32 (1): 245–65. https://doi.org/10.1016/j.emc.2013.10.002.

Endo, M. 2021. Review of *History of Medical Physics*. *Radiological Physics and Technology* 14 (November): 345–57.

E.W. Emery, "Geiger-Mueller and Proportional Counters" in *Radiation Dosimetry*, Vol. II, F.H. Attix and W.C. Roesch (eds.) Academic Press, New York, 1966.

Franck, P. 1957. *Philosophy of Science*. Englewood, N.J.: Prentice Hall, Inc.

Hendee, William. 1970. *Medical Radiation Physics*. 1st ed. United States: Year Book Medical Publishers, Inc.

Knoll, Glenn. 2010. *Radiation Detection and Measurement*. 4th ed. United States: John Wiley and Sons, Inc.

Møller, Anders P., and Timothy A. Mousseau. 2012. "The Effects of Natural Variation in Background Radioactivity on Humans, Animals and Other Organisms." *Biological Reviews* 88 (1): 226–54. https://doi.org/10.1111/j.1469-185x.2012.00249.x.

Pradhan, AS, JI Lee, and JL Kim. 2008. "Recent Developments of Optically Stimulated Luminescence Materials and Techniques for Radiation Dosimetry and Clinical Applications." *Journal of Medical Physics* 33 (3): 85. https://doi.org/10.4103/0971-6203.42748.

Price, W.J. *Nuclear Radiation Detection*. 2nd ed., New York, McGraw-Hill, 1964.

Scharf, Waldemar, and Francis T Cole. 1996. *Particle Accelerators and Their Uses. Pt. 1 Accelerator Design*. Amsterdam Harwood.

Shahbazi-Gahrouei, Daryoush, Samaneh Setayandeh, and Mehrdad Gholami. 2013. Review of *A Review on Natural Background Radiation*. *Advanced Biomedical Research* 2 (1): 65.

Sharpe, J. 1964. *Nuclear Radiation Detectors*. 2nd ed. London: Methuen and Co.

Strydom, W., W. Parker, and M. Olivares. 2005. *Radiation Oncology Physics : A Handbook for Teachers and Students*. Edited by Podgoršak, Ervin. Vienna: International Atomic Energy Agency. pp. 273-299, Chapter 8: Electron Beams: Physical and Clinical Aspects

United States Nuclear Regulatory Commission. 2017. "NRC: Radiation Basics." Nrc.gov. 2017. https://www.nrc.gov/about-nrc/radiation/health-effects/radiation-basics.html.

Wilkinson, D.H. 1950. *Ionization Chambers and Counters*. London: Cambridge University Press.